Prediction of perforation into concrete accounting for saturation ratio influence at high confinement

J Baroth, M Briffaut, D Vu, Y Malecot, L. Daudeville

To cite this version:

J Baroth, M Briffaut, D Vu, Y Malecot, L. Daudeville. Prediction of perforation into concrete accounting for saturation ratio influence at high confinement. International Journal of Impact Engineering, 2021, 156, pp.Article 103923. 10.1016/j.ijimpeng.2021.103923 . hal-03272104

HAL Id: hal-03272104

https://hal.univ-grenoble-alpes.fr/hal-03272104v1

Submitted on 28 Jun 2021

HAL is a multi-disciplinary open access archive for the deposit and dissemination of scientific research documents, whether they are published or not. The documents may come from teaching and research institutions in France or abroad, or from public or private research centers.

L'archive ouverte pluridisciplinaire **HAL**, est destinée au dépôt et à la diffusion de documents scientifiques de niveau recherche, publiés ou non, émanant des établissements d'enseignement et de recherche français ou étrangers, des laboratoires publics ou privés.

Manuscript File Click here to view linked References

Prediction of perforation into concrete accounting for saturation ratio influence at high confinement

J. Baroth, M. Briffaut, D. Vu, Y. Malecot, L. Daudeville

Univ. Grenoble Alpes, CNRS, Grenoble INP, 3SR, F-38000, Grenoble, France

Abstract

This paper provides both an analytical and a finite element model aiming at better predicting possible perforation of reinforced concrete slabs submitted to impacts. Both models account for free water saturation ratio and high triaxial stress induced into concrete by the impact. Finite element simulations are performed with Abaqus explicit code using a revised constitutive model for concrete; this coupled damage plasticity model (PRM) accounts for strain rate effects and the influence of saturation ratio on the triaxial behavior. Complementary original analytical predictions of ballistic limit and residual velocities are provided for both hard and soft impacts. These predictions depend on a recent deviatoric stress-based formulation of compressive strength of concrete. Numerical and analytical results are consistent with bending and punching experimental tests.

Keywords: soft and hard impacts, residual velocity, reinforced concrete, perforation capacity, saturation ratio

---

* Corresponding author.
E-mail address: jbaroth@univ-grenoble.fr (J. Baroth).

1. Introduction

In the past decades, some experimental campaigns have been conducted in order to better understand the response of concrete structures under extreme loads such as explosion or impacts and also to propose new design methods. Some of these experimental campaigns consisted in missile impact tests on reinforced concrete (RC) slabs. Among others, one can quote Meppen tests [1], [2], Vulcain tests [3-5], or the Iris benchmark (Improving Robustness Assessment Methodologies for Structures Impacted by Missiles) [6] and more recently Xu et al works [7]. Some papers published after Iris benchmark provided finite element simulations of all these tests [8-13]. They highlighted different features influencing simulation results such as material models (concrete and steel), strain rate effects, concrete fracture energy or erosion value. Little available data on concrete material properties is a cause of discrepancies between numerical and experimental results [14]. To have a better the knowledge of the concrete behavior, unconfined compression tests and triaxial compression tests at confining pressures up to 100 MPa have then been conducted on the IRIS high performance concrete (HPC) by Chung et al. [12] and Vu et al. [15].

The effect of free water on concrete mechanical behavior has been studied under high or moderate strain rates [16-19]. However, the effect of free water on the mechanical behavior of concrete under high stress level is still an investigate topic, essentially due to a lack of experimental data. In particular, numerical investigations recently investigated the influence of free water content using advanced constitutive models for concrete, in case of thick concrete targets under ogival-nosed projectile impact [20, 21]. These works emphasize that the water-saturation ratio is shown to be a major parameter that needs to be taken into account for predicting the ballistic performance of concrete targets.

The authors of the present study were the first who experimentally highlighted the effect of free water on the maximum deviatoric stress that concrete material can withstand [22,15]. They also measured the interstitial pore pressure during a triaxial test and showed that it may reach about the same value as the confining pressure [23]. Consequently, the prediction of the perforation resistance of concrete structures under impacts requires accounting for the influence of free water content on concrete behavior, especially when these structures are massive, their drying process being then very slow.

Thus, Vu et al. [15] conducted triaxial compression tests on IRIS HPC samples with various saturation ratios. Vu et al. also carried out tests under very high confining pressure (600 MPa) in order to highlight the important effect of the saturation ratio at high mean stress. Only the PRM FE model [24] based on the effective stress concept [25] was proposed to model wet concrete response under very high stress level. Thanks to these tests performed on IRIS HPC

[12] [15], the coupled damage plasticity model PRM proposed by Pontiroli et al. [24] had been slightly revised [15]. This last version accounts for strain rate, Lode angle and tensile damage [26].

In the present paper, the revised PRM model is used to simulate Iris impact tests; numerical and experimental results are compared. Following this study and using recent works [5], [27], analytical predictions for the ballistic limit and residual velocities are derived. Section 2 recalls briefly the analytical formulation proposed by Baroth et al. [5] and the revised PRM constitutive model for concrete. Section 3 presents Iris tests (hard and soft impacts) and in section 4 failure patterns and penetration resistance of concrete slabs are predicted thanks to a transient dynamic finite element analysis. The revised PRM model allows better predicting experimental results than the original model. Finally, section 5 provides and compares experimental results to analytical predictions of ballistic limits and residual velocities for various saturation ratios. It also gives complementary numerical results for soft impacts. Main notations of the paper are gathered in Table 1.

Table 1
Main physical quantities and parameters used.

Symbol	Parameter	Unit	Symbol	Parameter	Unit
M_p	*Projectile mass*	kg	f_{ck}	*Compressive strength of concrete (28 days, uniaxial)*	Pa
M_C	*Concrete mass (ejection cone)*	kg	σ_T	*Compressive strength (target)*	Pa
u	*Crushed length*	m	σ_x , σ_m	*Principal and mean stresses*	Pa
			q	*Deviatoric stress*	Pa
u^*	*Characteristic crushed length*	m	q_{max}	*Maximum deviatoric stress*	Pa
F_P	*Projectile crushing force*	N	q_1	*Critical shear stress of dry concrete*	Pa
A_P	*Crushed projectile cross-section*	m²	$\sigma_{c_{p0}}$	*Ultimate consolidation stress*	Pa
e_P	*Projectile thickness*	m	σ_{tot}	*Total stress*	Pa
r_{P1}	*Projectile mean radius*	m	b	*Biot coefficient*	-
V_0, V_C	*Projectile velocity before impact, ballistic limit*	m/s	p	*Pore pressure*	Pa
V_{res}	*Residual velocity*	m/s	ε_v	*Volumetric strain*	-
V_C^S	*Ballist limit for soft impact*	m/s	λ	*Entrained air coefficient*	Pa
u_P, u_T	*Displacements of the*	m	κ	*Capillary porosity*	Pa

	projectile and target			*coefficient*	
ρ_p	*Projectile mass density*	kg/m^3	Sr	*saturation ratio*	%
d	*Projectile diameter*	m	M_a	*Reinforcement density*	kg/m^3
L	*Projectile length*	m			
υ	*Poisson's ratio of steel*	-	ρ_C	*Concrete mass density*	kg/m^3
E	*Young's modulus of steel*	Pa	e_T	*Target thickness*	m
f_y	*Yield strength*	Pa	e_T	*Perforation limit*	m

2. Perforation capacity of concrete slabs under soft impacts

This section summarizes the analytical formulation to predict perforation of RC slabs [5] and the main features of the revised PRM constitutive model [15].

2.1 Analytical perforation prediction in case of soft impacts

In case of hard impact, various empirical formulae were proposed to predict the ballistic limit or the penetration depth into concrete and RC targets. Among them, Berriaud et al. [26] proposed a perforation limit formula, whose range of validity has been extended later [29], taking into account the missile nose shape influence. The effects of the projectile nose shape on the extent of local damage were also investigated experimentally in case of soft impact [30]. In such case, recent experimental and numerical studies improve the understanding of failure mechanisms in reinforced concrete targets, e.g. [31, 32]. But to the best of authors' knowledge, no analytical formula was proposed except for the prediction of the ballistic limit by Baroth et al. [5]. This formula is based on the distinction between hard and soft impacts proposed by Koechlin & Potapov [33]; the formula allows determining the crushed length u of the deformable missile:

$$u = \mathrm{Max}\left(0, \frac{M_P}{2F_P}\left((V_0)^2 - \frac{\sigma_T - F_P / A_p}{\rho_p}\right)\right) \ldots \textbf{(2.1)}$$

where M_p, V_0 are the projectile mass (kg) and the initial projectile velocity (m/s) respectively, σ_T is the compressive strength of the target (MPa), ρ_p the mass density (kg/m^3), F_P , A_P are the crushing force (N) and the crushed projectile cross-section (m^2) respectively.

If the possible crushed length u of the missile is greater than the characteristic crushed length ($u > u*$), the dissipated energy during crushing is too high, compared to projectile initial kinetic energy to allow perforation. Or else, if the possible crushed length is not long enough ($u < u*$), the dissipated energy during crushing is not high enough to stop the projectile; there is perforation.

Berriaud's model [26] or derived ones are based upon the uniaxial compressive strength after 28 days. Baroth et al. [4] and Zingg et al. [34] have shown that latter parameter is a poor indicator of concrete compressive strength under high confinement. For that reason, the present paper proposes for hard impact an approach based upon the deviatoric strength of concrete that depends on its composition and its saturation ratio [27].

2.2 Revised PRM constitutive model

The PRM coupled model has been developed in order to deal with computational problems of structures subjected to impact or blast loading [34]. It is based on a coupling between a damage model and the KST plasticity model initially developed for soils [35] and modified in [36]. It includes the calculation of the effective stress defined for a wet concrete to take into account the influence of free water content on the response of concrete [25]. The damage model is based on two damage variables, in compression and tension respectively, in order to simulate the unilateral feature of concrete behavior. In the revised model used in this paper [15], a poro-mechanical approach is used to take into account the effect of free water. The studied porous medium is assumed to be composed of a solid phase (skeleton) and a fluid phase occupying the voids [37]. The classical concept of effective stress is introduced to distinguish the stress in the solid phase with the pore water pressure.

$$\sigma_{tot} = \sigma_M + bp \ldots\mathbf{(2.2)}$$

with σ_{tot} the total stress, σ_M the stress transmitted through the matrix at macroscopic scale,

p the pore water pressure, and b the Biot coefficient which depends on the nature of the porosity. As the material reaches the consolidation point (closure of all the pores not filled with water), the volumetric behavior remains nonlinear because voids filled with water continue to be compacted due to the water compressibility (see [15]). But even if the consequences of the improvements have been shown at the material scale, the assessment of their effects on the numerical prediction of the global response of a concrete slab submitted to impact loading was not carried out.

3 Presentation of Iris tests

Impact tests were carried out by the Finnish VTT laboratory. Two types of cylindrical projectiles (length L and diameter d) were launched on rectangular RC slabs of thickness e_T mass density ρ_T. Projectiles and slabs have been designed to simulate hard and soft projectile impacts.

3.1 Projectiles

The first type of projectile, for hard impact, is filled with concrete and the second type, for soft impact, is hollow. Their characteristics are gathered in **Table 2**. Projectiles considered for soft impacts are metallic cylinders, whose lowest thickness is 3 mm over a length of 1 m. Two tests were conducted with initial velocities equal to 110 and 112 m/s [14]. The crushing force for this part is around 540 kN. Taking into account the effect of strain rate, this force is found around 630 kN [14].

Projectiles used for hard impacts are filled with light concrete cast one month before the test. Their outer diameter is 168 mm. Three tests, denoted a, b, c, were conducted with initial velocities around 135 m/s. The rear part of the projectile consists of an aluminum bar that allows measuring the residual velocity of the perforating projectile by a system of cameras installed behind the slab.

Table 2

Projectiles description: cylinders filled with concrete and hollow cylinders [6,14]

Symbols	*Parameters*	*Punching test (hard impact)*	*Bending test (soft impact)*
L, d	*Missile size (m)*	*0.64 (L) × 0.1683 (d)*	*2.11 (L) × 0.254 (d)*
e_P, l_P	*Thickness (over the length)*	-	*3 mm (1 m)*
	Concrete inside	*yes*	*no*
M_p	*Missile mass (kg)*	*47.38*	*49.99*
f_y, E, υ	*Characteristics of steel: Yield limit, Young's modulus, Poisson's ratio*	*235 MPa, 200 GPa, 0.3 (steel EN1.4432)*	
V_0	*Initial velocity (m/s) (Tests a ; b ; c)*	*135.85; 134.86; 136.46*	*110.15; 111.56*

3.2 Reinforced concrete slabs

Square RC slabs with 2.1 m side length are used. Thicknesses of slabs are 15 and 25 cm for soft and hard impacts respectively. Displacement sensors are located on the front face of the slab to measure displacements at various points (see **Fig. 1**). Each test was carried out at least twice to assess the test reproducibility that was verified in terms of fracture patterns, slab displacements, rebar deformations, projectile residual velocities. The slabs for hard impacts (25 cm thick) are reinforced by two A500HW steel reinforcement layers with a 10 mm diameter (**Fig. 2**). The distance between 2 rebars is 90 mm, their length is 1.025 m and the concrete cover thickness is 30 mm. These slabs have no transverse reinforcement to facilitate the projectile perforation.

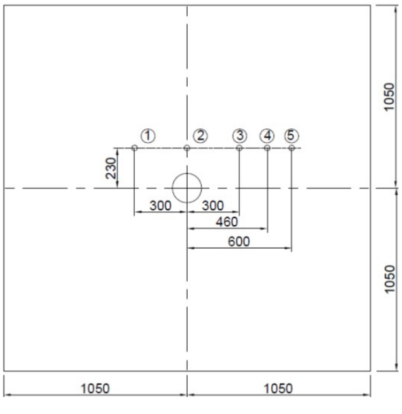

Fig. 1. Positions of displacement sensors on the target front face (perforation test).

Fig. 2. Concrete slab reinforcement.

3.3 Concrete properties

The Iris concrete is representative of that selected for a nuclear reactor building (67 MPa unconfined compressive strength and 4.5 MPa tensile strength, see composition in **Table 3**).

Table 3
Concrete composition and properties.

Concrete mix (for 1 m^3)	
Gravel (0.5/8) (kg)	925.9
Sand (kg)	646.1
Water (kg)	215
Cement (CEM II B 42.5) (kg)	489
Fly ash (kg)	88
Superplasticizer (kg)	6.33
Density (kg/m^3)	2260
Main concrete properties	
Unconfined uniaxial compressive strength (28 days) (MPa)	67
Porosity accessible to water (%)	12
Cement paste volume (m^3 for 1m^3 of concrete)	0.375
Water/Cement ratio	0.44

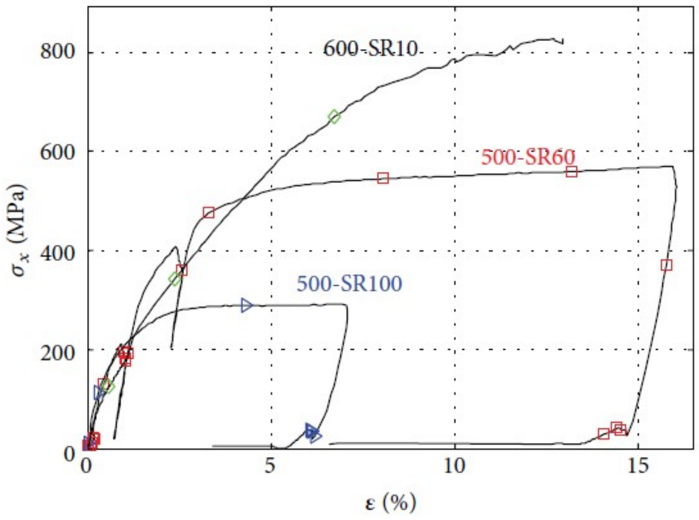

Fig. 3. Axial behavior, comparison of stress-strain curves under triaxial compression at high confinement for various saturation ratios (circles: *Sr* = 10%; squares: *Sr* = 60%; triangles: *Sr* = 100%) [15].

Triaxial compression tests were performed on Iris fully saturated concrete samples with triaxial confining pressures up to 100 MPa [6]. In addition, Vu et al. [15] performed tests at very high confining pressure and various saturation conditions (500 MPa - 60%; 600 MPa - 10%). **Figure 3** displays test results given by Vu et al. [15]; it shows the stress-strain curve of 3 samples with various saturation ratios *Sr* = 10, 60 and 100% under triaxial compression at high confinement (500 and 600 MPa). Under high confinement, the compressive strengths reach values varying between 250 and more than 800 MPa for *Sr* = 100 and 10% respectively. Vu et al. [15, 22] explain that the strength loss of wet concrete is due to the interstitial water pressure effect. Under moderate confinement, the material is not compacted enough to close the voids and to provoke an interstitial water pressure effect. Consequently, no influence of free water on the concrete behavior is observed, as modelled by [38]. The influence of free water appears only under dynamic loading with significant strain-rate effect [39, 40].

4. Finite element modeling of the perforation test

4.1. Finite element discretization

Given the double symmetry of the system, only a quarter of the slab is modelled. The projectile shown in **Fig. 4** is a 168 mm diameter steel tube filled with lightweight concrete. Its length is 64 cm. Since the thin hollow metallic cylinder has no influence, 3D finite elements (C3D8R) are used to mesh the projectile; the weight of one quarter of the projectile is 11.75 kg.

Fig. 4. Mesh of a quarter of projectile and slab [15].

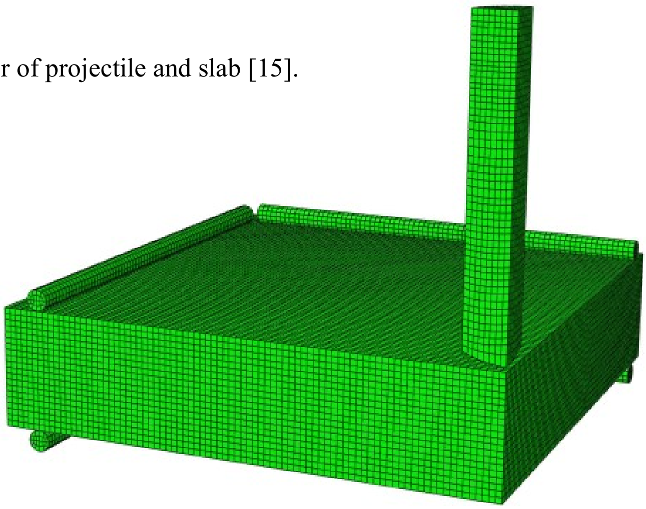

The concrete finite element mesh is homogeneous with a 12.5 mm element size. This mesh refinement has been chosen, knowing that PRM model uses Hillerborg et al. regularization technique [41] and that the non-mesh dependency of PRM model has been shown in [42]. We also remind that this macroscopic constitutive behavior for concrete accounts for strain-rate in tension. In compression, strain-rate effect due to inertia is accounted in the 3D FE modeling. The concrete plate consists finally of 129,488 C3D8R finite elements. The rebars are modeled using 2-node beam elements with a circular cross-section (see **Table 4**). The 10 mm rebars are meshed with 3608 beam elements. The reinforced concrete slab is surrounded by a U shape metal frame that is modelled using 11632 C3D8R elements of the same size as the concrete elements. The thickness of this frame is 25 mm. It is supported by steel cylinders that block the displacement but allow a possible rotation.

Table 4
Characteristics of rebars and of half slabs.

Geometry of slab / Type of test	*Punching*	*Bending*	*Unit*
Slab dimensions (two directions)	*1.05*		*m*
Thickness of the slab (e_T)	*25*	*15*	*cm*
Reinforcement density (M_a)	*54.6*	*105*	*kg/m³*
Rebar diameter	*10*		*mm*
Rebar number (two directions)	*12*		
Concrete coating	*20*		*mm*

4.2. Simulation results

In this section, simulation results obtained either with the original coupled PRM model or with the revised coupled PRM model are compared. **Figure 5** shows the projectile and the deformed slab at time 30 ms (end of the impact test, Fig. 5a). **Figure 5b** also displays the numerical evolution of the projectile velocity for both models (i.e. before and after improvement) during a perforation test into a fully saturated RC slab. Both calculations are blind simulations. From this figure one can conclude that the perforation prediction is significantly improved with the revised PRM model; the predicted residual velocity is close to the experimental one.

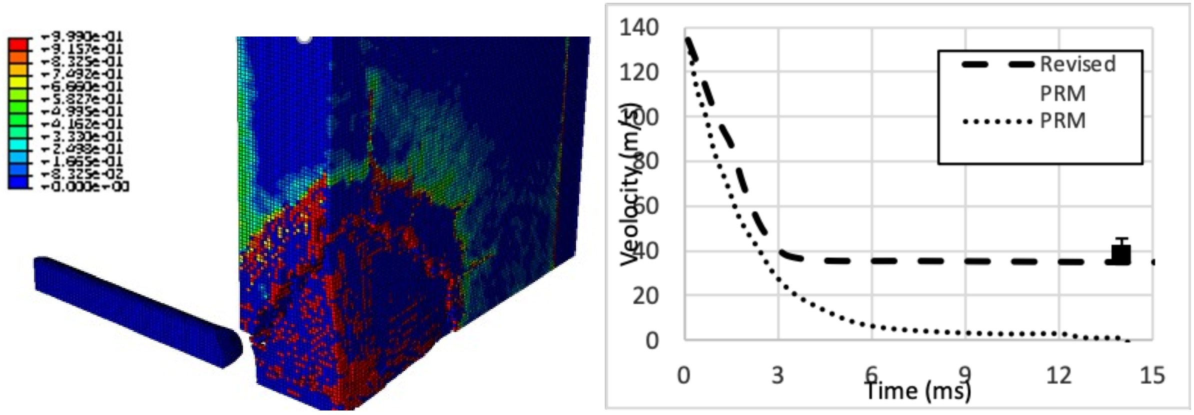

a) *b)*

Fig. 5. Numerical results using revised PRM, accounting for free water: projectile and the deformed slab at time 30 ms corresponding to the end of the impact test (a), experimental and numerical evolutions of the projectile velocity (b).

Table 5 provides numerical predictions of residual velocities at low saturation ratios, which cannot be compared with experimental results and will serve as reference for the analytical prediction described in the next paragraph.

Table 5
Experimental and numerical residual velocities for different saturation ratios.

	Exp	*Sr* ≈ 99% (num)	*Sr* ≈ 80% (num)	*Sr* ≈ 40% (num)	*Sr* ≈ 0% (num)
Residual velocity (m/s)	33.8	35.18	16.73	12.21	11

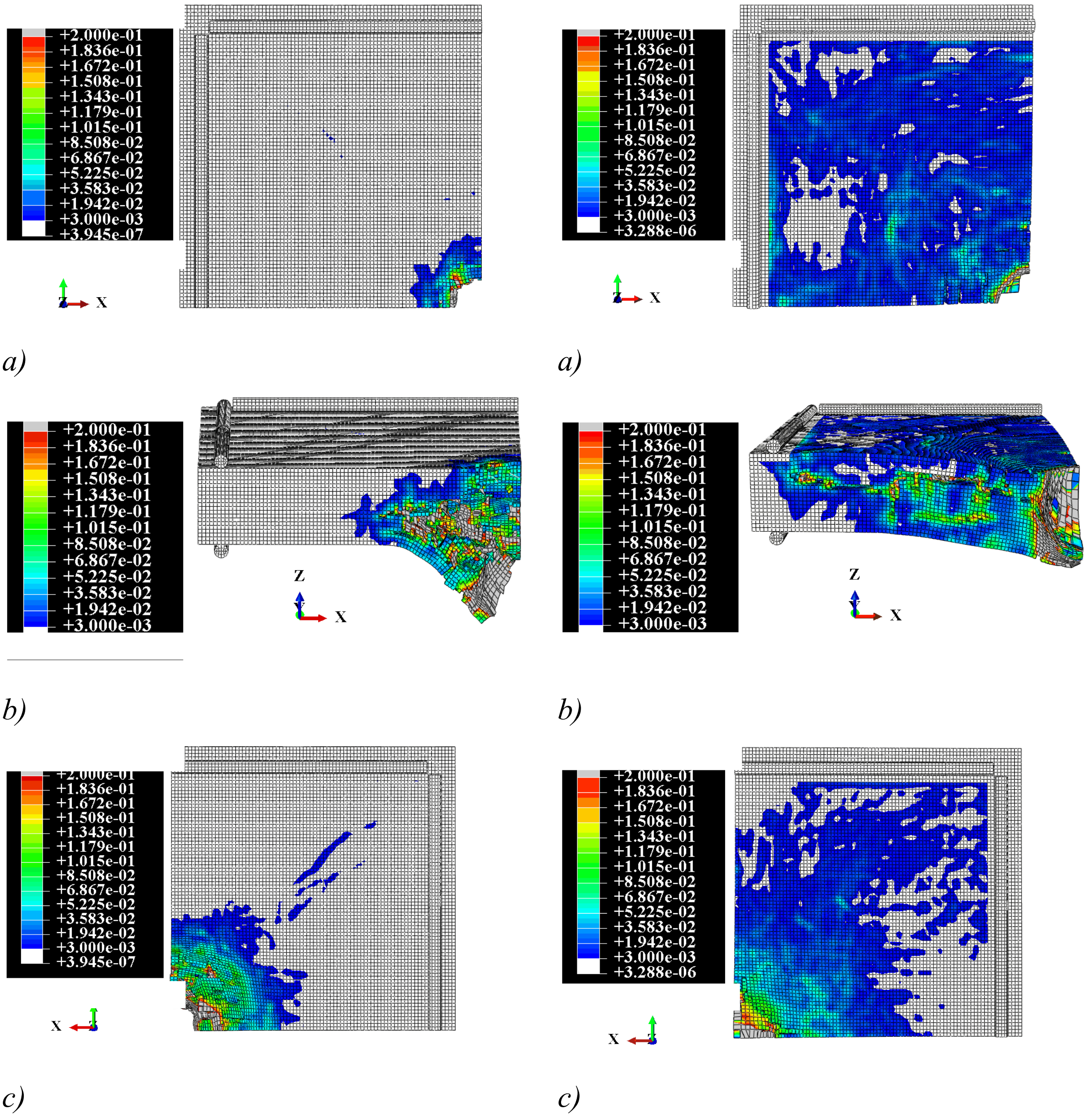

a) *a)*

b) *b)*

c) *c)*

Fig. 6. Maximal principal strain with the revised PRM model at the end of the perforation simulation: Front face (a), cross section (b), rear face (c).

Fig. 7. Maximal principal strain with the original PRM at the end of the perforation simulation: Front face (a), cross section (b), rear face (c).

(a) (b)

Fig. 8. Experimental observed failure patterns of punching test (IRIS Benchmark [6]): font face (a), rear face (b).

The effect of the model revision on the fracture pattern can be observed on **Fig. 6** and **Fig. 7**. The original PRM leads to a larger plasticity zone (See **Fig. 7**), whereas the revised PRM model allows activating the damage in the impact zone more extensively (**Fig. 6)**. This failure pattern is closer from the experimental one that can be seen on **Fig. 8** and leads to a higher residual velocity (**Fig. 5**).

5. Analytical prediction of the perforation (soft and hard impacts)

In this section, analytical predictions of ballistic and residual velocities are discussed. The analytical estimation depends on the ultimate compressive strength of the target σ_T , which itself depends on the saturation ratio, as illustrated in **Fig. 3.** In the following, the strength of concrete is estimated according to Malecot et al. [27], who propose to consider the maximum deviatoric stress.

5.1. Prediction of the maximum deviatoric stress for Iris concrete

Malecot et al. [27] defined an empirical evolution of the maximum deviatoric stress q_{max} in concrete depending on its composition and its porosity (See Appendix). This formula has been developed from several concrete compositions with some of them are close to those of

Iris concrete. **Table 6** displays predictions of the maximum deviatoric stress q_{max} versus the saturation ratio Sr according to this formula for Iris concrete.

Table 6
Maximum deviatoric stress q_{max} (S_r) (MPa), for different saturation ratios for two concretes using empirical formula defined in [27]

	f_{ck} (MPa)	$Sr \approx 99\%$	$Sr \approx 80\%$	$Sr \approx 40\%$	$Sr \approx 0\%$
Iris [15]	67	300	406	738	1217
[24]	28.7	214	329	692	1217

5.2. Ballistic and residual velocities in case of hard impacts (punching tests)

For these tests, the cylindrical part of projectiles is filled by concrete and thus considered as rigid. Berriaud's formula [22] can then be used to predict the ballistic limit.

$$V_c^2 = 1.89 f_{ck} \left(\frac{f_{ck}}{\sigma_0} \right)^{-1/2} \rho_T^{1/3} \left(\frac{d e_T^2}{M_P} \right)^{4/3} N^2 \left(0.35 \left(\frac{M_a}{M_{a0}} \right)^{0.7} + 0.65 \right)^2 \quad \text{... } \mathbf{(5.1)}$$

where f_{ck} is the uniaxial compressive strength of concrete after 28 days (MPa), M_a the reinforcement density (kg/m^3), M_P the projectile mass (kg), e_T the thickness of the target (m), N the nose shape factor and M_{a0}, σ_0 constants.

Nevertheless, the latter formula is based on the uniaxial compressive strength of the target that is a poor indicator of concrete impact strength. This parameter does not account for the effect of water saturation or high confinement conditions [24]. In Eq (5.1) f_{ck} is thus replaced by q_{max} (S_r) and the factor $1.89 f_{ck} \left(\frac{f_{ck}}{\sigma_0} \right)^{-1/2}$ in Eq (5.1) is replaced by $a(q_{\max} - q^*)^{1/2}$ with a and q^* to be identified from [24] and Iris tests results (see **Table 6**).

$$V_c^2 = a \sqrt{q_{\max} - q^*} \rho_T^{1/3} \left(\frac{d e_T^2}{M_P} \right)^{4/3} N^2 \left(0.35 \left(\frac{M_a}{M_{a0}} \right)^{0.7} + 0.65 \right)^2 \quad \text{... } \mathbf{(5.2)}$$

The resulting analytical residual velocity is then obtained considering the kinetic energy balance, accounting for mass loss, whose influence can be significant [31]:

$$V_{res} = \sqrt{\frac{M_P(V_0^2 - V_C^2)}{M_P + M_c}} \; ... \; \mathbf{(5.3)}$$

where M_c is the ejected concrete mass, estimated from the formula given in [43], which gives a reasonable order of magnitude:

$$M_c = \frac{\pi}{3}(r^2 + r_c^2 + r.r_c)x \; \rho_T \; ... \; \mathbf{(5.4)}$$

where ρ_T is the mass weight of the concrete, r is the radius of the hole created in the slab, $r_c = (d+3{,}5e_T)/2$, and x equal or less than e_T.

The estimation of the residual velocity is concluded applying Eqs. (5.2)-(5.4), with values of parameters that can be found in **Tables 2, 3, 4** and **7**, for saturated concrete (*Sr* =100 %).

Table 7
Parameters used to apply Eqs. 5.2-5.4 to estimate the residual density (Eq. 5.3) for *Sr*=100%

Symbol	*Parameter*	*Value*	*Unit*
N	*Nose shape factor*	1.18	-
σ_0	*Reference compressive strength*	36.6	MPa
M_{a0}	*Reference reinforcement density*	200	kg/m^3
M_a	*Reinforcement density*		
a	*Fitting parameter*	7389	-
q^*	*Fitting deviatoric stress*	139.2	MPa

This formula allows comparing this analytical residual velocity with experimental and FE estimations (see **Table 5**) for a saturation ratio close to 100 %. One can see in **Fig. 9** that this analytical residual velocity appears in the average of experimental velocities.

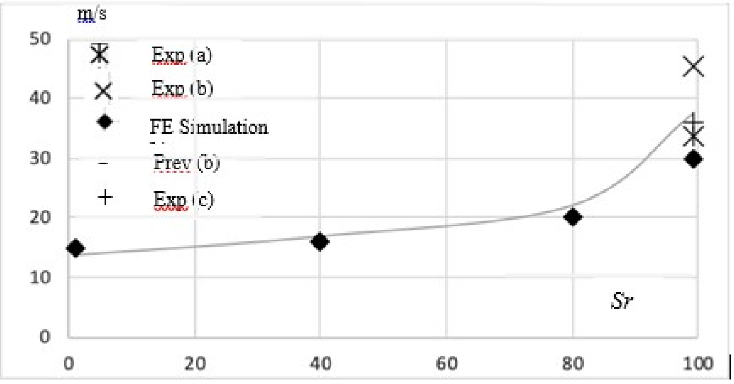

Fig. 9. Experimental, numerical and analytical residual velocities.

For non-saturated targets, no experiment has been carried out. Only the FE and analytical predictions can be compared. In this case, to account for the saturation ratio influence, the analytical ballistic velocity is written as:

$$V_c^2 = a\sqrt{\alpha q_{\max} - q^*}\,\rho_c^{1/3}\left(\frac{de_Y^2}{M_P}\right)^{4/3} N^2\left(0.35\left(\frac{M_a}{M_{a0}}\right)^{0.7} + 0.65\right)^2$$

… **(5.5)**

with $\alpha = \alpha(q_{\max}(Sr))$ the saturation ratio influence factor defined such that

$$\alpha(q_{\max}) = \left(bq_{\max}^2 + cq_{\max} + d\sqrt{q_{\max}} + e\right)\ldots\textbf{(5.6)}$$

where (*b, d, c, d*) are fitting parameters respectively found equal to ($4.93.10^{-6}$, -0.0235, 0.821, -6.85).

5.3. Case of soft impacts (bending tests)

In case of soft impact, the ballistic limit V_C^S has been proposed in [5]. It takes into account the crushed length *u* of the projectile (m), its crushing force (N) of the finest part of the projectile, denoted F_P, and the hard impact ballistic limit V_C (m/s), such that

$$V_C^S = \sqrt{V_C^2 + \frac{2F_P u}{M_P}} \quad \ldots \textbf{(5.7)}$$

Perforation occurs when $u \geq u^*$, defined as the characteristic crushed length (Eq. 2.1). This length has been defined in [5] depending on the uniaxial compressive strength f_{ck}. Accounting for the maximal deviatoric stress q_{max}, this length is define as:

$$u = \mathrm{Max}\left(0, \frac{M_P}{2F_P}\left((V_0)^2 - \frac{q_{\max} - F_P / A_p}{\rho_p}\right)\right) \ldots \textbf{(5.8)}$$

where M_p, V_0 are the projectile mass (kg) and the initial projectile velocity (m/s) respectively, ρ_p the mass density (kg/m^3), F_P, A_P are the crushing force (N) of the finest part of the projectile and the crushed projectile cross-section (m^2) respectively.

Two estimations of the crushing strength, with and without strain-rate effect, are reported in **Table 8**, in order to estimate the crushed length. Ballistic limits defined in Eqs. 5.5 and 5.7

are also provided. The estimated crushed length is clearly closer to experimental measures if the strain effect is taken into account.

Table 8
Comparison between experimental and analytical predicted characteristics for Iris soft impacts

Characteristics	Experiments	Predictions		
	Soft impact	*Soft impacts*		*Hard impact*
Crushing force (kN)	unknown	540 kN [14]	630 kN with strain rate effet [14]	-
Velocities (m/s)	(*initial velocities*) $V_0 = 110.1–111.6$ m/s	*(estimated* $V_C^S = 126.8 –$ 127.4 m/s	*ballistic* $V_C^S = 140.2 –$ 140.8 m/s	*limits)* $V_C = 86$ m/s
Crushed length	96 - 98 cm	80 – 82 cm	97 - 99 cm	-

6. Conclusion

This study has proposed numerical and analytical studies of impact tests (punching and bending) on RC slabs, conducted by OECD/NEA IAGE working group (Iris 2010 and 2012 benchmark projects). Both hard and soft impact analyses have been performed. Analytical estimations of ballistic and residual velocities have been proposed. The originality of these estimations is to account for a realistic triaxial compression strength. For hard impact, the residual velocity prediction is based on a kinetic energy balance and an analytical formula inspired by Berriaud's regression formula which gives the ballistic limit. The material strength of concrete used in this analytical formula is not the unconfined compressive strength but the maximum deviatoric strength that depends on the water saturation ratio. In case of soft impact, this strength is also used to predict the ballistic limit and the crushed lengths of the deformable projectiles. Predicted analytical crushed lengths are closer to experimental ones if the strain rate effect is taken into account.

The hard impact test has also been modeled with the finite element code Abaqus explicit using the revised PRM constitutive model for concrete, accounting for strain rate effects and the saturation ratio. The comparison of FE and experimental results clearly show a better prediction of failure patterns. The FE model allows correctly predicting the residual velocity of the projectile for saturated concrete slabs, but also provides estimations of concrete slab response for different saturation ratio values. Numerical and analytical estimations are consistent thanks to a saturation ratio influence factor accounted in the analytical formula.

7. Acknowledgments

This research has been partially performed with the financial support of CEA Gramat and IRSN. Authors also thank the Research Centre of Finland VTT for kindly providing test results to all benchmark participants.

8. References

[1] Jonas W., Meschkat R., Riech H., Rüdiger E., « Experimental investigations to determine the kinetic ultimate bearing capacity of reinforced concrete slabs subject to deformable missiles », *Proc. 5th SMiRT*, Berlin, Germany, 1979, J8/3.

[2] Nachtsheim W., Stangenberg F., « Interpretation of results of Meppen slab tests – Comparison with parametric investigations », *Nuclear Engrg and Design*, vol. 75, n°2, 1982, p. 283-290.

[3] Pontiroli C, Rouquand A, Baroth J, Daudeville L. Soft projectile impacts analysis on thin reinforced concrete slabs: Tests, modelling and simulations, European J of Environmental and Civil Eng 2012;16:1058-1073.

[4] Baroth J, Daudeville L, Malecot Y, About empirical models predicting the missile perforation of concrete barriers, European J of Environmental and Civil Eng 2012;16(3):1074-1089.

[5] Baroth J., Malecot Y., Boukria Z., Briffaut M., Daudeville L., Prediction of the perforation of targets impacted by deformable projectiles, *International J. of Impact Engrg*, 2015:80, 36-44.

[6] NEA. Iris_2010, Improving robustness assessment methodologies for structures impacted by missiles, workshop proceedings, IRSN editor, 2010.

[7] Xu, L., Cai, F., Xue, Y. *et al.* Numerical Analyses of Local Damage of Concrete Slabs by Normal Impact of Deformable Solid Projectiles. *KSCE J Civ Eng* **23,** 5121–5132 (2019).

[8] Martin O., Centro V., Schwoertzig T., Finite element analysis on the Meppen-II-4 Slab Test, Nuclear Engineering and Design 247 (2012) 1– 10.

[9] Martin O., Centro V., Schwoertzig T., Finite element analysis on the VTT–IRSN flexural failure test, Nuclear Engineering and Design 252 (2012) 88– 95.

[10] Orbovic N., Sagals G., Blahoianu A., Influence of transverse reinforcement on perforation resistance of reinforced concrete slabs under hard missile impact, Nuclear Engineering and Design 295 (2015) 716–729.

[11] Orbovic N., Tarallo F., Rambach J.-M., Sagals G., Blahoianu A., Iris 2012 OECD/NEA/CSNI benchmark: Numerical simulations of structural impact, Nuclear Engineering and Design 295 (2015) 700–715.

[12] Chung C., Leea J., Jung R., Numerical simulations of missile impacts on reinforced concrete plates: Iris-2010/2012 benchmark project, Nuclear Engineering and Design 295 (2015) 747–758.

[13] Lee H.-K., Kim S.-E. Structural behavior of SC panel subjected to impact loading using finite element analysis, Nuclear Engineering and Design 295 (2015) 96–105.

[14] Moore J et al. Iris 2010 International Benchmark, Improving robustness assessment methodologies for structures impacted by missiles, workshop proceedings, Working Group of components and structures, report of team ENSI / B&H, IRSN editor, 2010.

[15] Vu X.D., Briffaut M.,Malecot Y., Daudeville L. and Ciree B., Influence of the Saturation Ratio on Concrete Behavior under Triaxial Compressive Loading, Hindawi Publishing Corporation *Science and Technology of Nuclear Installations,* vol 2015, Article ID 976387, 10 p.

[16] Rossi P., Van Mier J. G. M., Boulay C., Le Maou F. (1992). The dynamic behaviour of concrete: influence of free water. Materials and Structures, 25(9), 509-514.

[17] Zhou J., Chen X., Wu L., Kan X. (2011). Influence of free water content on the compressive mechanical behaviour of cement mortar under high strain rate. Sadhana, 36(3), 357.

[18] Wu S., Chen X., Zhou J. (2012). Influence of strain rate and water content on mechanical behavior of dam concrete. Construction and Building Materials, 36, 448-457.

[19] Sun X., Wang H., Cheng X., Sheng, Y. (2020). Effect of pore liquid viscosity on the dynamic compressive properties of concrete. Construction and Building Materials, 231, 117143.

[20] Forquin, P, Sallier L., Pontiroli C. , A numerical study on the influence of free water content on the ballistic performances of plain concrete targets, *Mechanics of Materials*, Vol. 89, 015 , pp 176-189

[21] Zhao FQ, Wen HM., Effect of free water content on the penetration of concrete, *International J. of Impact Engrg,* Vol 121 , 2018 , pages 180-190

[22] Vu X.H., Malecot Y, Daudeville L, Buzaud E., « Experimental analysis of concrete behavior under high confinement: Effect of the saturation ratio », *International J. of Solids and Structures*, vol. 46, n°5, 2009, p. 1105-1120.

[23] Accary A., Malecot Y., Daudeville L. 2019. Design and evaluation of a deformable sensor for interstitial pore pressure measurement in concrete under very high stress level. Applied Sciences. 9(13): 2610

[24] Pontiroli C., Rouquand A., Mazars J., « Predicting concrete behaviour from quasi-static loading to hypervelocity impact. An overview of the PRM Model », *European J. of Environmental and Civil Engrg*, vol 14, n°6-7, 2010, p.703-727.

[25] Mariotti C., Perlat J.P., Guerin J.M., 2003. A numerical approach for partially saturated geomaterials under shock, Int. J. of Impact Engineering, 28: 717 - 741.

[26] Erzar, B., Pontiroli C., Buzaud E. Ultra-high performance fibre-reinforced concrete under impact: experimental analysis of the mechanical response in extreme conditions and modelling using the Pontiroli, Rouquand and Mazars model. Philosophical Transactions of the Royal Society A: Mathematical, Physical and Engineering Sciences, 2017, vol. 375, no 2085, p. 20160173.

[27] Malecot Y, Zingg, Briffaut M, Baroth J., Influence of free water on concrete triaxial behavior: The effect of porosity, Cement and Concrete Research 120 (2019) 207–216.

[28] Berriaud C, Dulac J, Sokolovsky A, Labrot R, Gueraud R, Avet-Flancard R. Local behaviour of reinforced concrete walls under missile impact, Nucl Eng Des, 1978;45(2):457-469.

[29] Berriaud C., Dulac J., Perrot J., Avet-Flancard R., Impact on concrete: Synthesis of French Studies, *Proc. 7th SMiRT*, Chicago, USA, 1983, paper n°J8/2.

[30] Ohno T., Uchida T., Matsumoto N., Takahashi Y., Local damage of reinforced concrete slabs by impact of deformable projectiles, Nuclear Engineering and Design 138(1) (1992) 45-52.

[31] Guo L., He Y., Zhang X.F., Pang C.X., Qiao L., Guan Z.W., Study mass loss at microscopic scale for a projectile penetration into concrete, International Journal of Impact Engineering 72 (2014) 17-25.

[32] Ardila-Giraldo O.A., Pujol S., Failure mechanisms of small-scale reinforced concrete beams impacted by soft missiles, Structures 20 (2019) 620-634

[33] Koechlin P, Potapov P. Classification of soft and hard impacts - Application to aircraft crash, Nucl Eng Des, 2009;239:613-618.

[34] Zingg L, Briffaut M, Baroth J, Malecot Y (2016) Influence of cement matrix porosity on the triaxial behaviour of concrete. Cem Concr Res 80:52–59.

[35] Krieg R.D., A simple constitutive description for soils and crushable foams, 1972.

[36] Swenson D.V, Taylor L.M., A finite element model for the analysis of tailored pulse stimulation of boreholes, Int. J. Numer. Anal. Methods Geomech. 7 (1983) 469–484

[37] Coussy O., 1995. Mechanics of Porous Continua, Wiley Ltd, New York.

[38] Benniou, H., Accary, A., Malecot, Y. *et al.* Discrete element modeling of concrete under high stress level: influence of saturation ratio. *Comp. Part. Mech.* (2020). https://doi.org/10.1007/s40571-020-00318-5

[39] Cadoni E., Labibes K., Albertini C., Berra M. and Giangrasso M., Strain-rate effect on the tensile behaviour of concrete at different relative humidity levels, Materials and Structures, Vol. 34, 2001, pp 21-26.

[40] Erzar B. and Forquin P., Experiments and mesoscopic modelling of dynamic testing of concrete, Vol. 43(9), 2011 , pp. 505-527

[41] Hillerborg A., Modéer M., Petersson P.-E. Analysis of crack formation and crack growth in concrete by means of fracture mechanics and finite elements. *Cement and concrete research*, 1976, vol. 6, no 6, p. 773-781.

[42] Mazars J., Dufour F., Giry C. Concrete under various loadings, way to model in a same framework: damage, fracture and compaction. Computational Modelling of Concrete Structures, 2010, p. 45-58.

[43] Hugues G., hard missile impact on reinforced concrete, *Nucl. Eng Des.*, 1984 ;77(1) :23-35.

[44] Vu X.H., Y. Malecot Y., Daudeville L., Buzaud E., Effect of the water/cement ratio on concrete behavior under extreme loading*, Int. J. Numer. Anal. Methods Geomech.*33 (17) (2009) 1867–1888.

9. Table captions

Table 1: Main physical quantities, their units and the coefficients used.
Table 2: Projectiles description: cylinder filled with concrete and hollow cylinder.
Table 3: Concrete properties.
Table 4: Characteristics of the rebars.
Table 5: Experimental and numerical residual velocities for different saturation ratios.
Table 6: Analytical maximum deviatoric stress for different saturation ratios
Table 7: Parameters used to apply Eqs. (5.2-4) to estimate the residual density (Eq. 5.3) for Sr=100%
Table 8: Comparison between experimental and analytical characteristics for Iris soft impacts
Table 11.1: Validity ranges for parameters used in Eq. (9.1) (min and max values) [5].
Table 11.2: Set of fitting parameters for the criterion [27].

10. Figure captions

Fig. 1: Position of displacement sensors on the front of the target (perforation test).
Fig. 2: Reinforcement in concrete slab.
Fig. 3: Axial behavior, comparison of the shear behavior of concrete for several saturation ratios (curve with circles: Sr = 10%; curve with squares: Sr = 60%; curve with triangles: Sr = 100%) [15].
Fig. 4. Mesh of a quarter of projectile and slab [15].
Fig. 5. Numerical results using revised PRM, accounting for free water: projectile and the deformed slab at 30 ms (a), experimental and numerical evolutions of the projectile velocity (b).
Fig. 6: Model with the revised PRM model: Front face (a), cross section (b), rear face (c).
Fig. 7: Model with the original PRM: Front face (a), cross section (b), rear face (c).
Fig. 8. Experimental observed failure of punching test (IRIS Benchmark [6]): font face (a), rear face (b).
Fig. 9: Experimental, numerical and analytical residual velocities.
Fig. 11.1: Hydrostatic behavior, oedometric behavior and consolidated behavior of concrete: mean stress in function of volumetric strain.
Fig. 11.2: Diagram of stress calculation according mixing theory poromechanical when concrete is consolidated.

11. Appendices

11.1. Analytical deviatoric stress in a concrete

Malecot et al. [27] proposed the following formula to represent the evolution of the maximum deviatoric stress in a concrete depending on its composition and its porosity. For a given saturation ratio S_r

$$q_{\max}(S_r) = q_0 - \frac{S_r}{2}(3 - \mathrm{S}_r)(q_0 - q_{sat}) \quad \textbf{…(11.5)}$$

with

$$q_0 \approx q_1\left(\frac{\sigma_{c_{p0}}}{q_1}\right)^{\alpha} \quad \textbf{…(11.6)}$$

and

$$q_{sat} \approx q_1\left(\frac{\sigma_{c_{p0}} - \lambda\phi_{air}^{1/3} - \kappa\phi_{cap}^{1/3} - f_{ck}/3}{q_1} + \left(\frac{f_{ck}}{q_1}\right)^{1/\alpha}\right)^{\alpha} \quad \textbf{…(11.7)}$$

with fitting parameters listed in Table 11.2

Table 11.2
Set of fitting parameters for the criterion [27].

Variable	Symbol	Value
Critical shear stress of dry concrete	q_1	980 MPa
Slope of the criterion on a logarithmic	α	0.81
Ultimate consolidation stress	$\sigma_{c_{p0}}$	1280 MPa
Entrained air coefficient	λ	210 MPa
Capillary porosity coefficient	κ	2350

Table 11.3
Compositions and mechanical properties

Concrete mix (for 1 m^3)	LPC	OC= EC06	HPC	EC04	EC08
Gravel (0.5/8 mm) (kg)	1008	1008	1008	1000	991
Sand (1.8 mm) (kg)	838	838	795.4	832	824
Water (kg)	169	169	140	136	181
Cement CEM II B 42.5 (kg)	263	263	420		
Cement CEM I 52.5 N PM ES CP2 (kg)				349	226
Silica fume (kg/m^3)	-	-	46.7	-	-
Entrained air agent (kg/m^3)	0.13	-	-		
Superplasticizer (kg)	-	-	4.7	4.5	
Density (kg/m^3)	2278	2277	2415	2322	2252
Slump (mm)	120	70	> 200	70	140
Uniaxial compressive strength at 28 days f_{ck} (MPa)	24	28.6	80	57	21
Accessible porosity to water (%)	10.8	11.8	8.8	7	14
Porosity measured by mercury intrusion (at 400 MPa)	15.6	12.6	8.7		
Entrapped air (measured on fresh concrete)	8.5	3.4	4.5		
Water/cement ratio	0.6	0.64	0.3	0.39	0.80

These formulae and parameters have been checked for five types of concretes considered herein (OC, HPC, LPC from [27], and EC04, EC08 from a previous study [44]). These concretes have very different unconfined compressive strengths and porosities, yet their granular stackings closely resemble one another.

All concrete mixes and main properties are listed in the table 11.3.

11.2 Improvement of PRM model (from Vu et al. [15])

11.2.1 Influence of the deviatoric stress on volumetric behavior

The plasticity model assumes that inelastic volumetric and shear strains are obtained independently. The volumetric strain ε_v is assumed to depend on just the mean stress σ_m, while the strain deviator tensor is obtained by means of a perfectly plastic damage model.

The effect of the deviatoric stress q on the volumetric behavior of concrete has therefore not been taken into account in the original PRM coupled model. This original model assumes that the compaction curve, i.e. the volumetric strain ε_v vs. mean stress σ_m curve, is obtained from material data independently of the loading path. [15] show that the inelastic volumetric strain depends on both q and σ_m, which suggests the necessity of including the influence of q in the material compaction curve (whereby ε_v is a function of (σ_m, q)).

To improve this PRM model, the curve depicting the volumetric behavior of concrete is not assumed to be bijective; instead, it is assumed bounded by both the hydrostatic and oedometric curves (**Fig. 11.1**). According to test results, it is indeed assumed that maximum compaction is obtained under an oedometric loading path. Under uniaxial strain conditions, concrete compaction is maximized because dilatancy is being prevented, whereas the hydrostatic loading path yields a lower compaction. The compaction curve oedometric test and the hydrostatic curve are then used as input data due to their ease of access by experimental measurement.

The variation in mean stress σ_m between the bounded curves is then given by:

$$d\sigma_m = \alpha \, d\varepsilon_v \qquad \textbf{…(11.8)}$$

with:

$$\alpha = \alpha_H + (\alpha_o - \alpha_H)\, Min\left[\left(\frac{\left(\frac{dq}{d\sigma_m}\right)}{\left(\frac{dq}{d\sigma_m}\right)_o}\right);1\right] \ldots \qquad \textbf{(11.9)}$$

where (see **Fig. 11.1**):

$\alpha_H = d\sigma_m/d\varepsilon_V$ obtained from a hydrostatic test;
$\alpha_O = (d\sigma_m/d\varepsilon_V)_O$ obtained from an oedometric test;
$dq \,/\, d\sigma_m$ = load path direction at the current Gauss point;

$(dq/d\sigma_m)_O$ = oedometric load path direction obtained from an oedometric test.

In formulae (11.10) and (11.11), the volumetric strain ε_v depends on both the mean stress σ_m and deviatoric shear stress q. A hydrostatic loading path contains no shear stress and its behavior follows the hydrostatic curve; however, for a current triaxial loading path with shear stress, the level of compaction is increased.

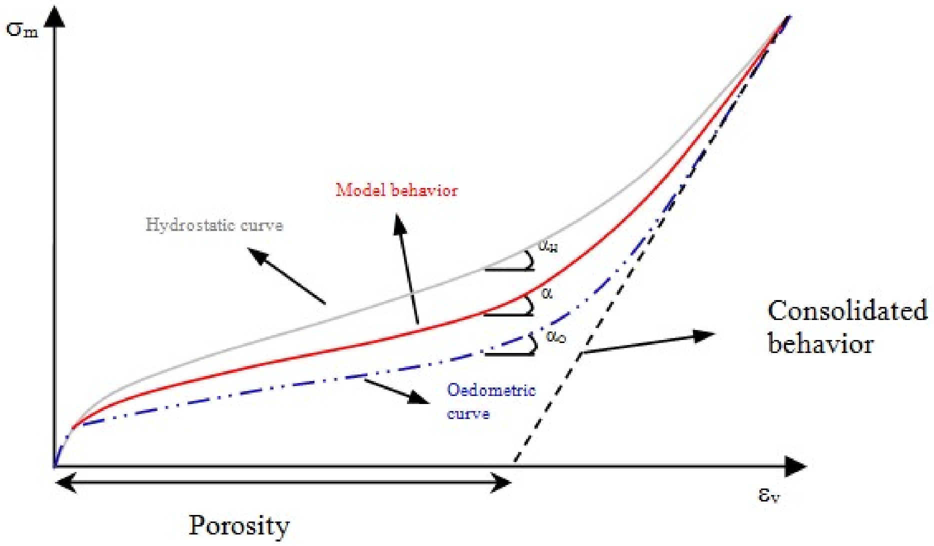

Fig. 11.1 Hydrostatic and oedometric constitutive behaviors and resulting triaxial behavior of concrete: mean stress vs. volumetric strain.

11.2.2. Influence of the water saturation ratio on volumetric behavior

Two types of approaches are available to characterize the behavior of a porous medium at its homogenized scale from microscopic-level properties. The "mixing law" approach takes into account, at the microscopic level, the interaction between the two phases (liquid + solid) by means of simple rheological models for each phase, whether associated in series or in parallel. Secondly, the poro-mechanical approach assumes that the mechanics concepts in a continuum mechanics are still valid at the macroscopic scale when the phases (liquid + solid) overlap.

In the original PRM coupled model, the concept of effective stress is applied to take into account the presence of water in confined concrete when using the first approach. The drawback with such an approach is that the material behavior becomes elastic after reaching the consolidation point (once all open pores are closed), which is not observed experimentally. In the revised model, the poro-mechanical approach allows taking the effect of free water into account.

The studied porous medium is assumed to be composed of both a solid phase (skeleton) and a fluid phase occupying the voids [37]. The concept of effective stress is introduced to separate fluid pressure in the total pressure calculation σ_{tot}, depending on the pore pressure p, based on the Mie-Grüneisen equation of state, i.e.:

$$p = \frac{\rho_0 C_0^2 \left(\varepsilon_V - \varepsilon_{Vps}\right)}{\left(1 - s\left(\varepsilon_V - \varepsilon_{Vps}\right)\right)^2} \left[1 - \frac{\Gamma_0 \left(\varepsilon_V - \varepsilon_{Vps}\right)}{2}\right] + \Gamma_0 \rho_0 E_M \qquad \textbf{...(11.10)}$$

where C_0 is the speed of sound in water (C_0 = 1,500 m/s), φ_0 the density (φ_0 = 1,000 kg/m^3 for water), s and Γ_0 two Mie-Grüneisen coefficients (s = 1.75 and Γ_0 = 0.28 for water), and E_M the internal energy per unit mass, with this energy being considered negligible for water temperature and ambient pressure.

The total pressure σ_{tot} also depends on the stress σ_M transmitted by the matrix at a macroscopic scale, and b the Biot coefficient which depends on the nature of the porosity.σ_M and b can be obtained by applying the following formulae:

$$\sigma_M = K_0\ \varepsilon_v \qquad \textbf{...(11.11)}$$

$$b = 1 - \frac{K_0}{K_S} \qquad \textbf{...(11.12)}$$

where K_0 is the modulus of the drained material, ε_V the volumetric strain at the homogenized scale, and K_S the compressibility modulus of the skeleton.

From Equation (11.4), in the particular case where $K_0 << K_s$, b is then close to 1, a result that simplifies Equation (2.2) and becomes $\sigma_{tot} = \sigma_M + p$ (i.e. Terzaghi's formula). In contrast, when $K_0 \approx K_S$ (case of dry concrete), b tends to 0. Thanks to homogenization of the drained porous medium, the ratio K_0/K_S can be estimated as follows:

$$\frac{K_0}{K_S} = (1-\phi)^3$$ **…(11.13)**

where ϕ is the porosity of the porous medium at the current state.

With this new hypothesis, whenever the material reaches the consolidation point (i.e. void pores become closed), the volumetric behavior remains nonlinear given that the voids filled with water continue to be compressed under compaction. Another advantage of this model improvement is the unique consolidation point instead of two points in the original PRM model (**Fig. 11.2**).

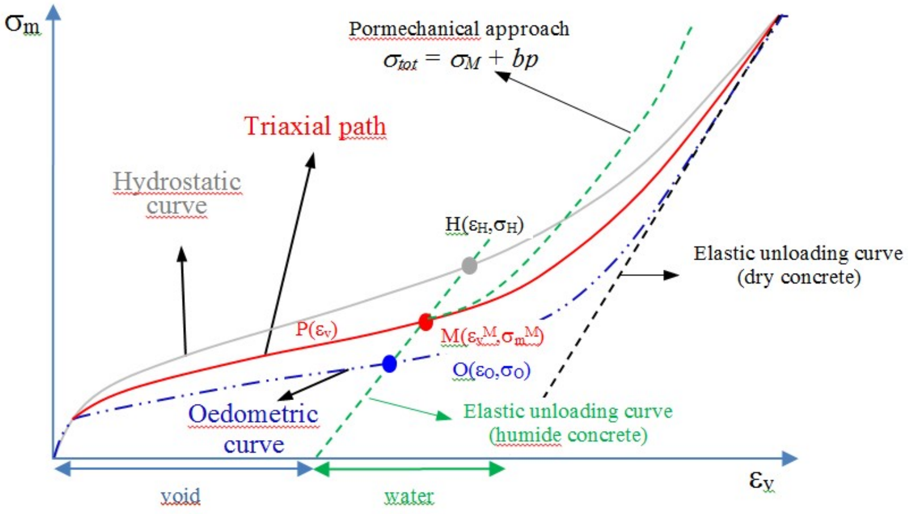

Fig. 11.2 Stress calculation diagram according to the poro-mechanical approach, as the concrete consolidates.

Click here to access/download;Figure;Fig1.png

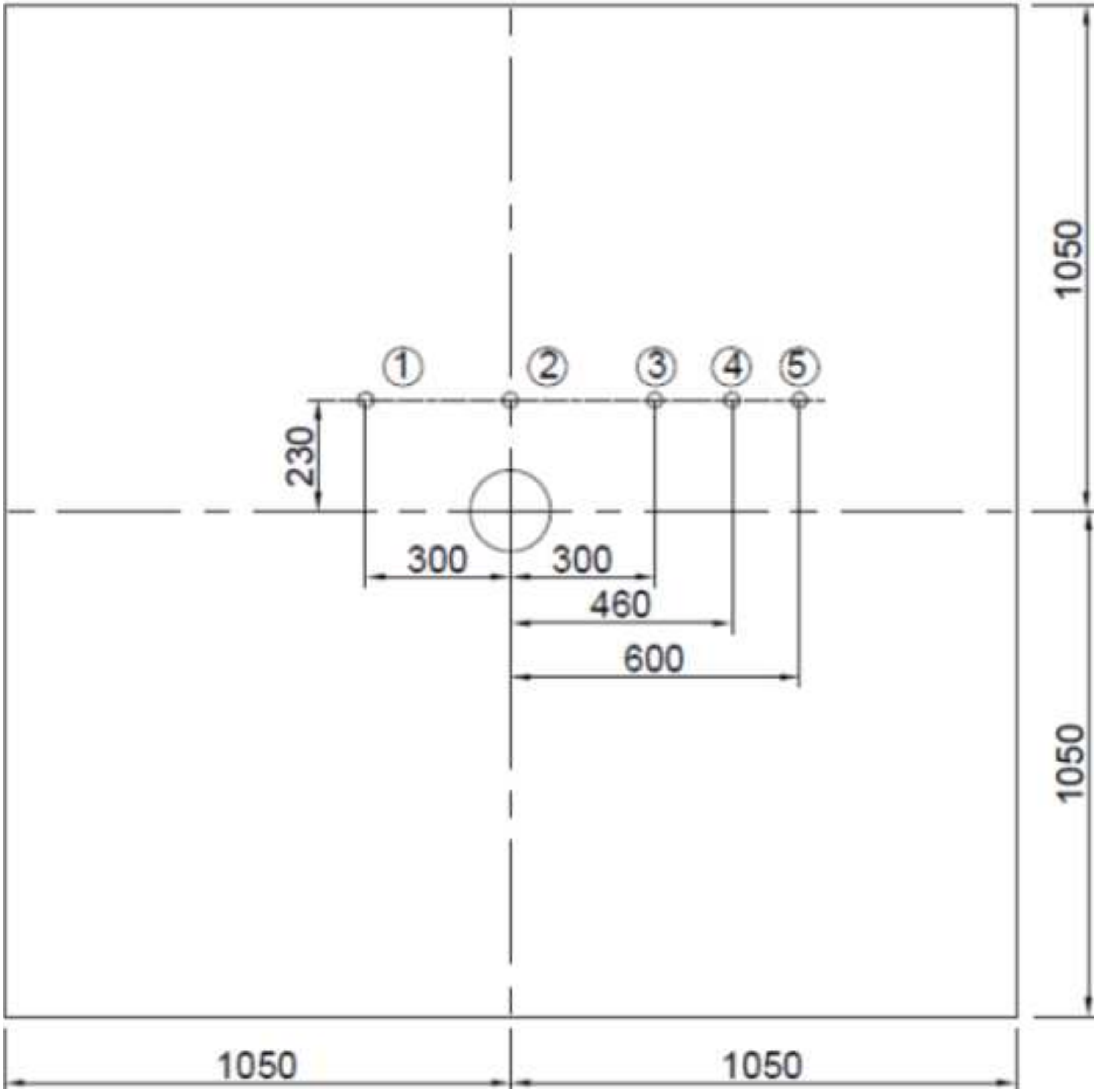

Click here to access/download;Figure;Fig2.png

Click here to access/download;Figure;Fig3.png

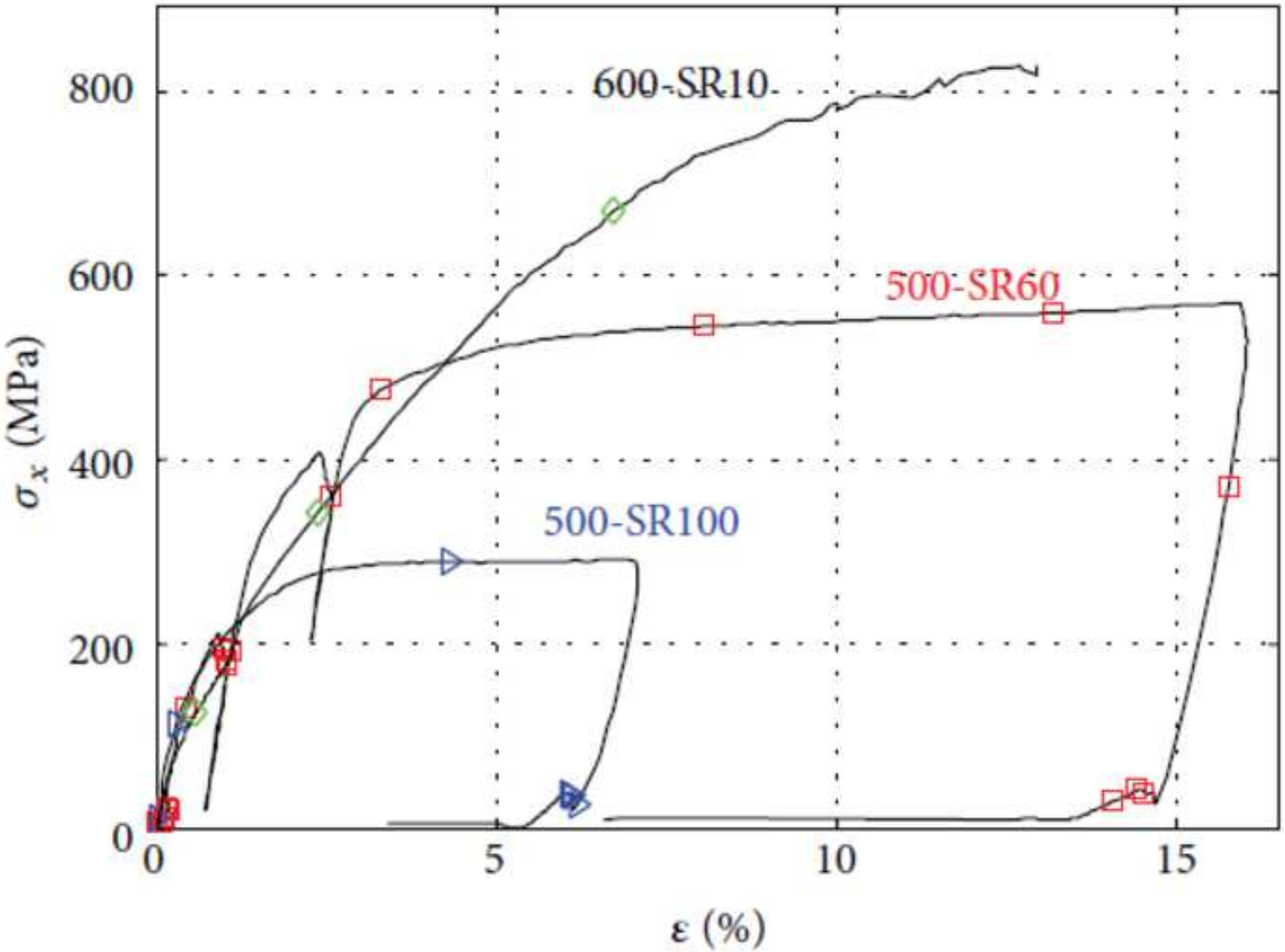

Click here to access/download;Figure;Fig4.png

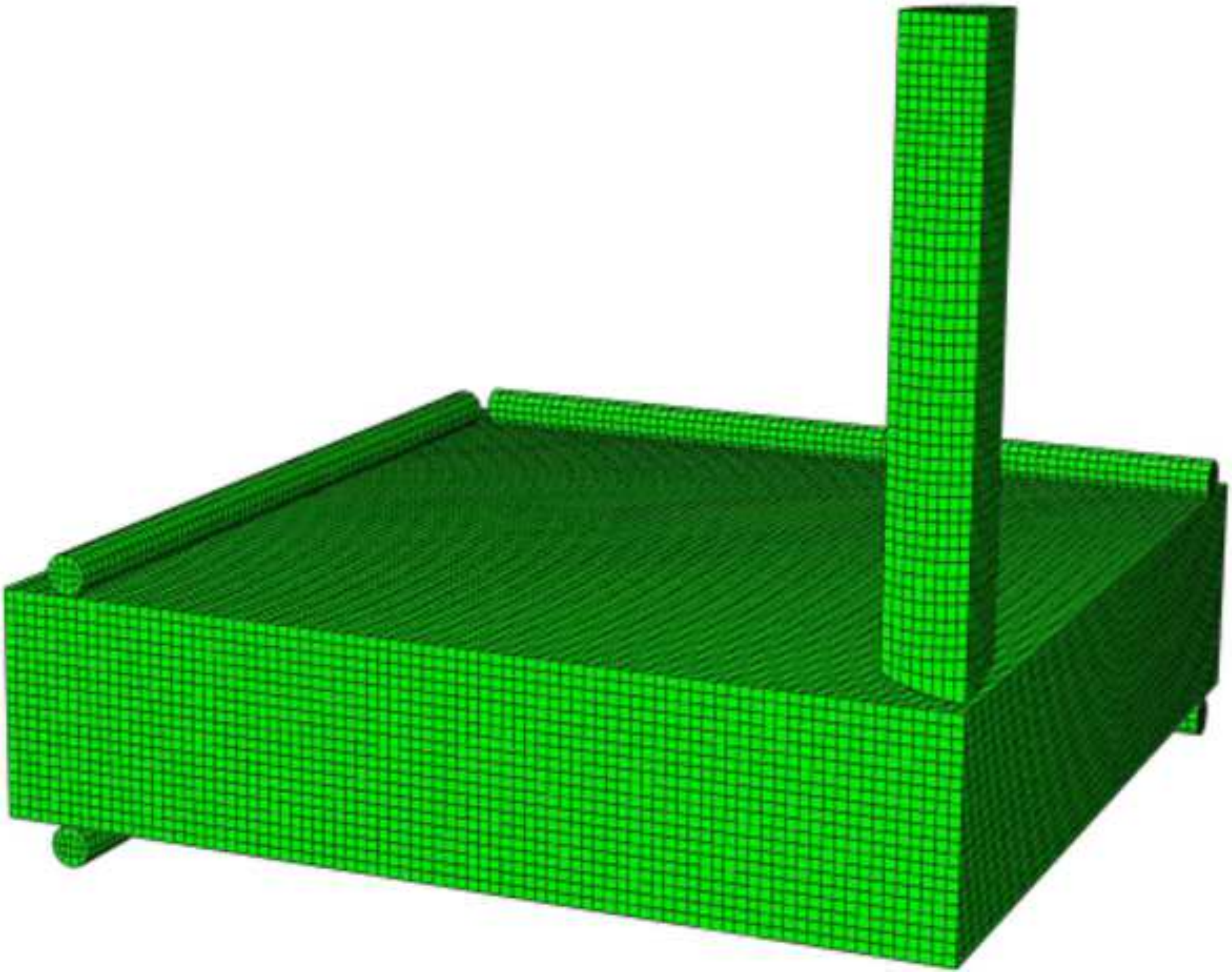

Figure Click here to access/download;Figure;Fig6a.png

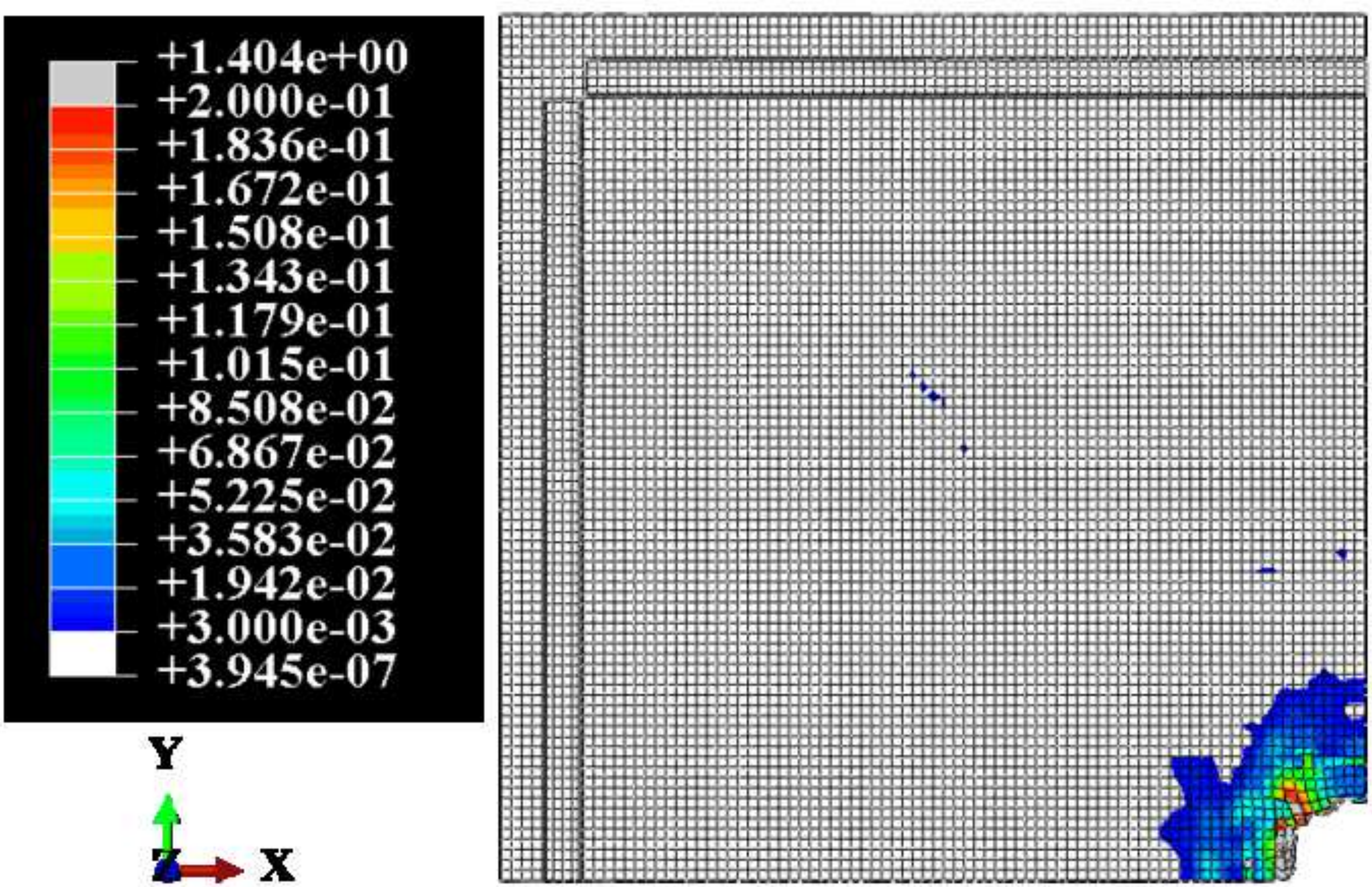

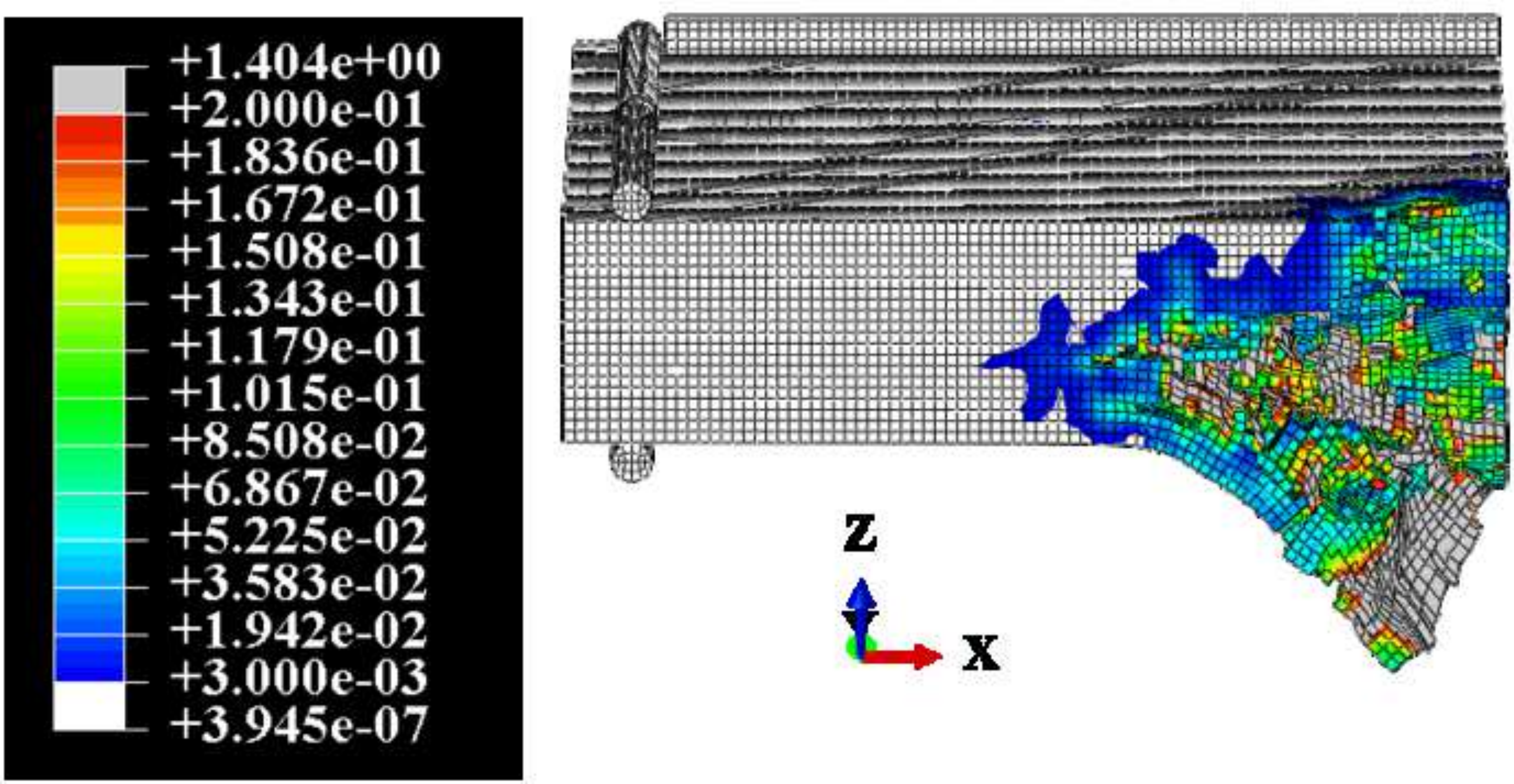
+1.404e+00
+2.000e-01
+1.836e-01
+1.672e-01
+1.508e-01
+1.343e-01
+1.179e-01
+1.015e-01
+8.508e-02
+6.867e-02
+5.225e-02
+3.583e-02
+1.942e-02
+3.000e-03
+3.945e-07
Z
X

Figure Click here to access/download;Figure;Fig6c.png

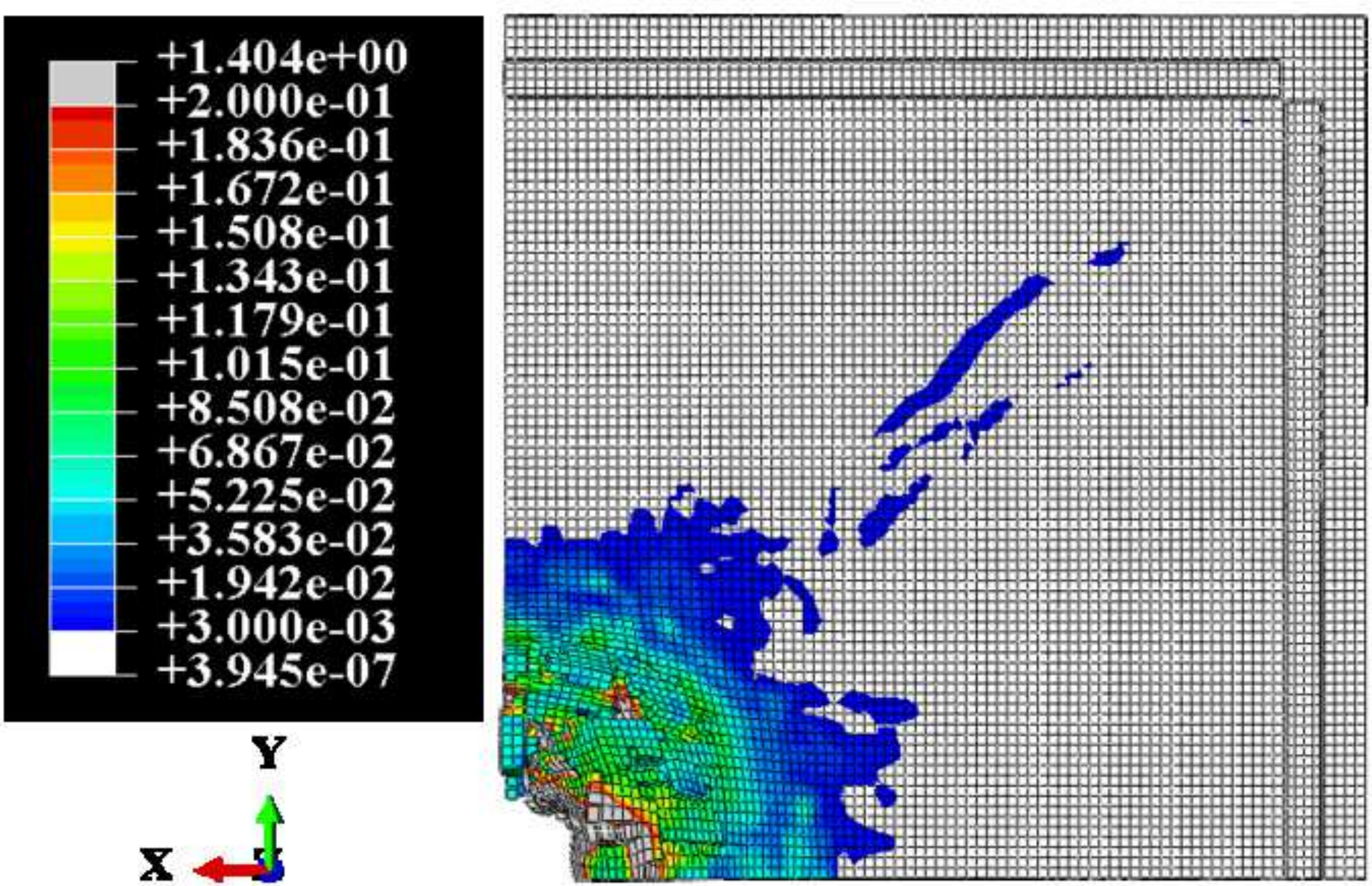

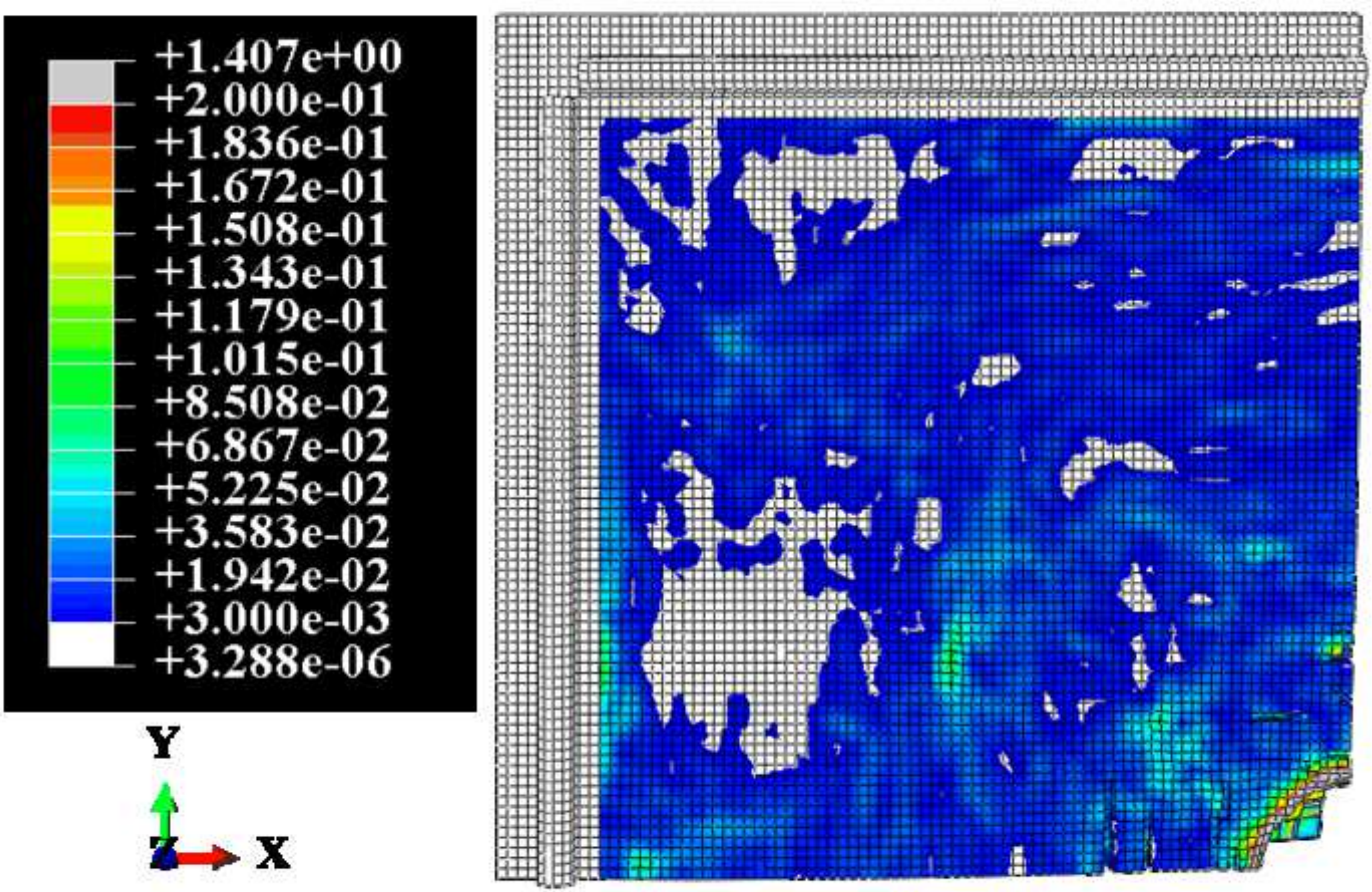
+1.407e+00
+2.000e-01
+1.836e-01
+1.672e-01
+1.508e-01
+1.343e-01
+1.179e-01
+1.015e-01
+8.508e-02
+6.867e-02
+5.225e-02
+3.583e-02
+1.942e-02
+3.000e-03
+3.288e-06
Y
Z
X

Figure

Click here to access/download;Figure;Fig7b.png

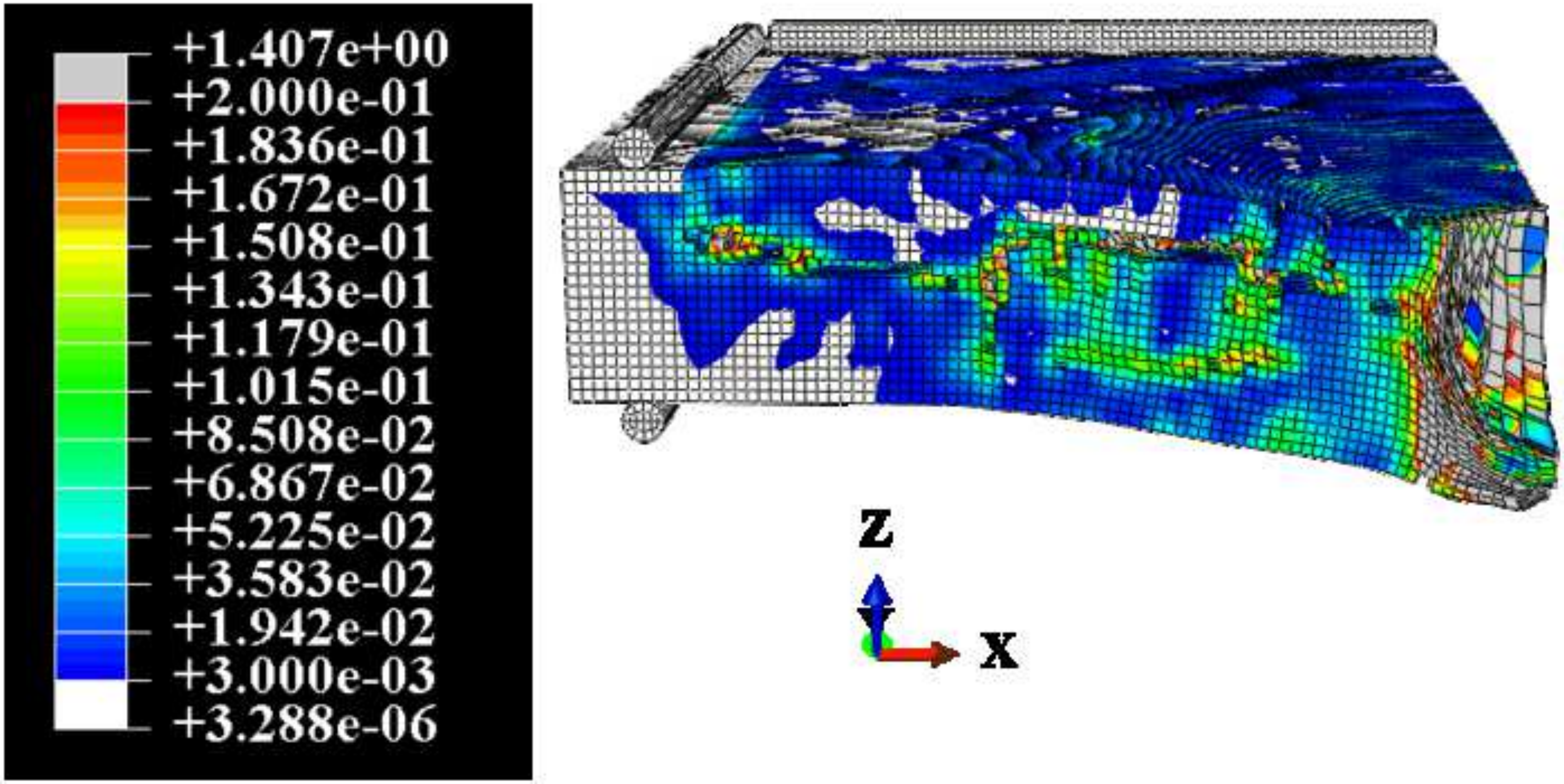

Click here to access/download;Figure;Fig7c.png

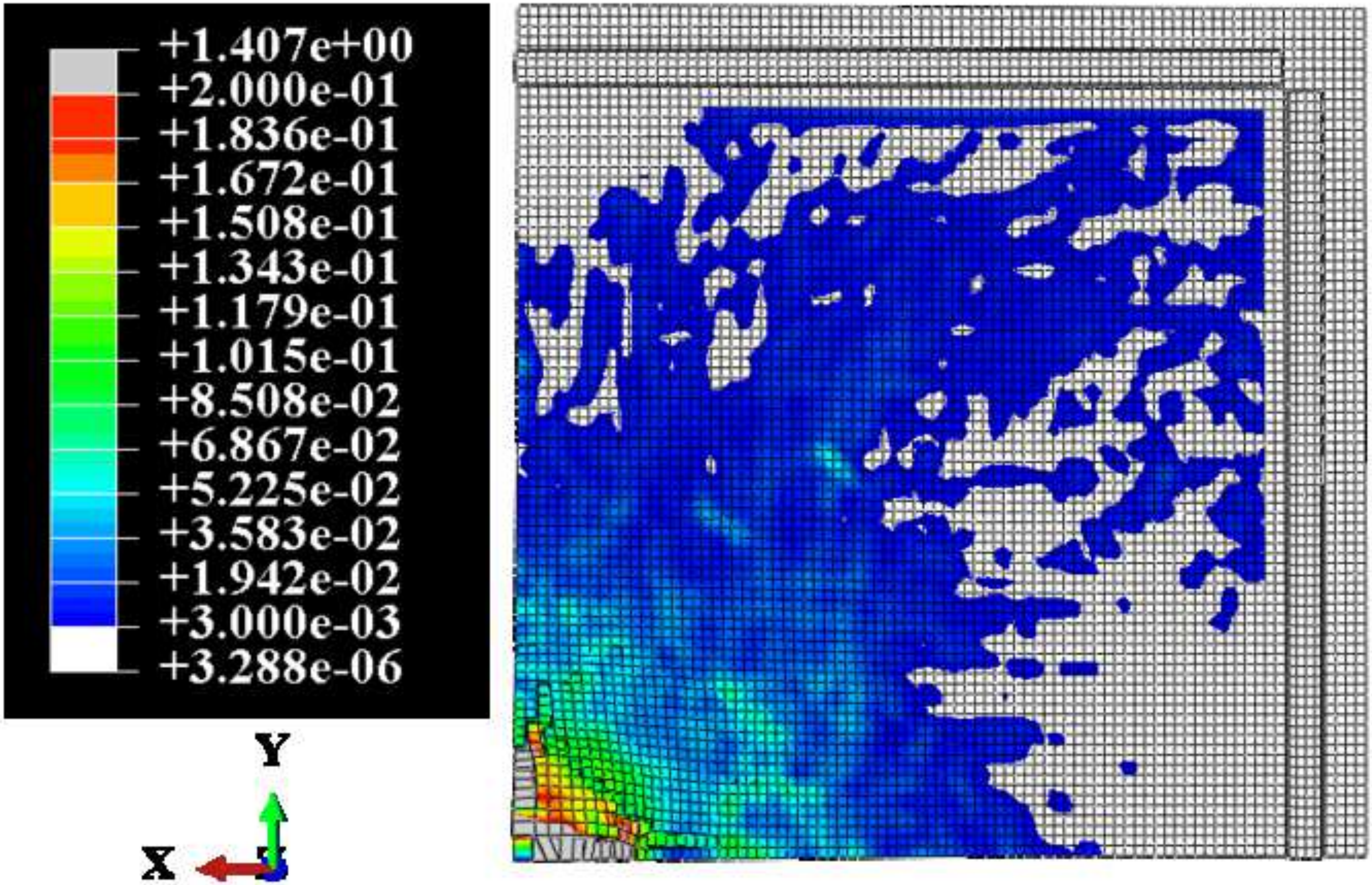

Figure Click here to access/download;Figure;Fig111.png

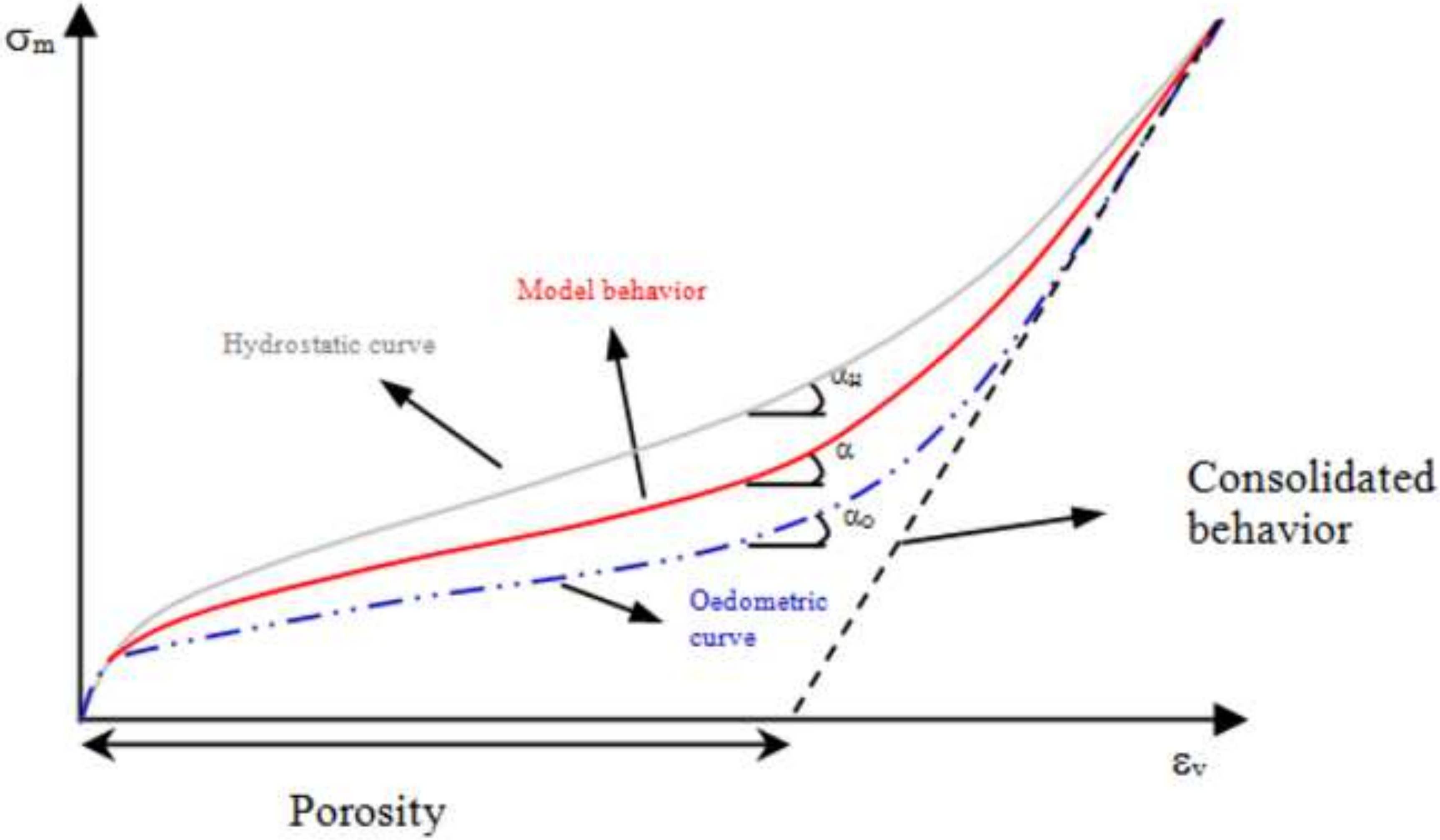

Figure Click here to access/download;Figure;Fig112.PNG

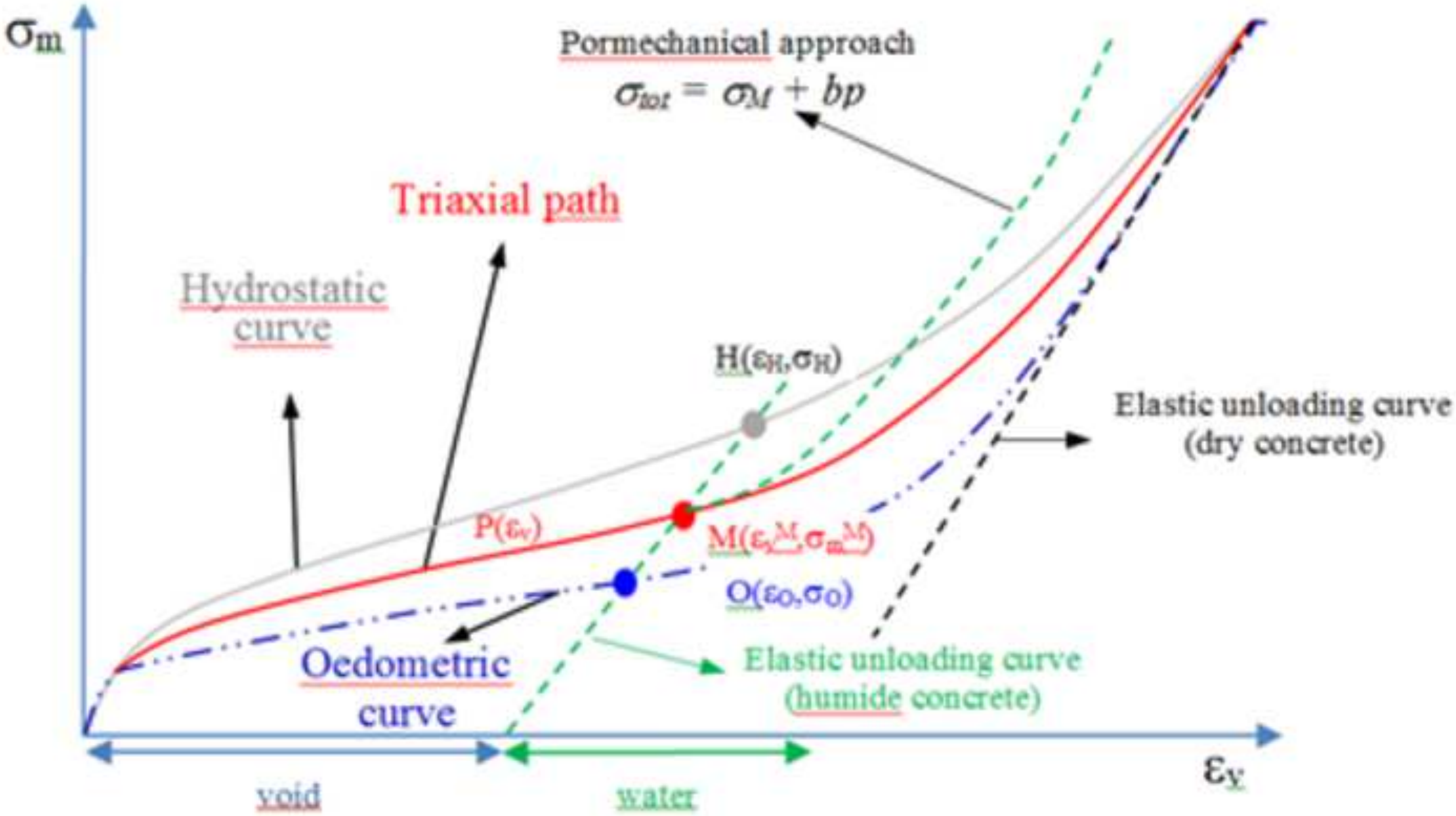

Figure

Click here to access/download;Figure;Fig8b.PNG

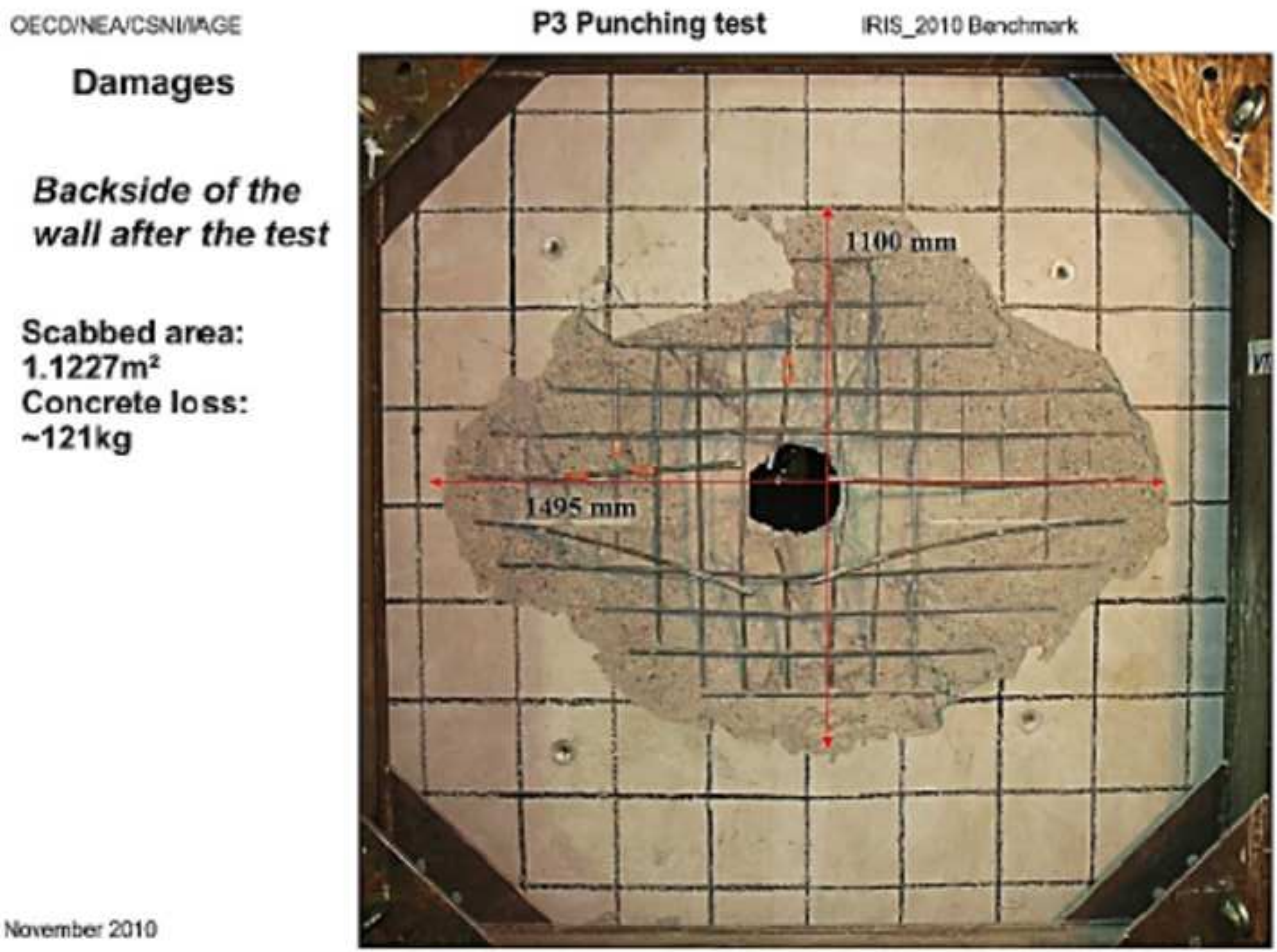

OECD/NEA/CSNI/IAGE

P3 Punching test

IRIS_2010 Benchmark

Damages

Backside of the wall after the test

Scabbed area:
1.1227m^2
Concrete loss:
~121kg

November 2010

Click here to access/download;Figure;Fig8a.PNG

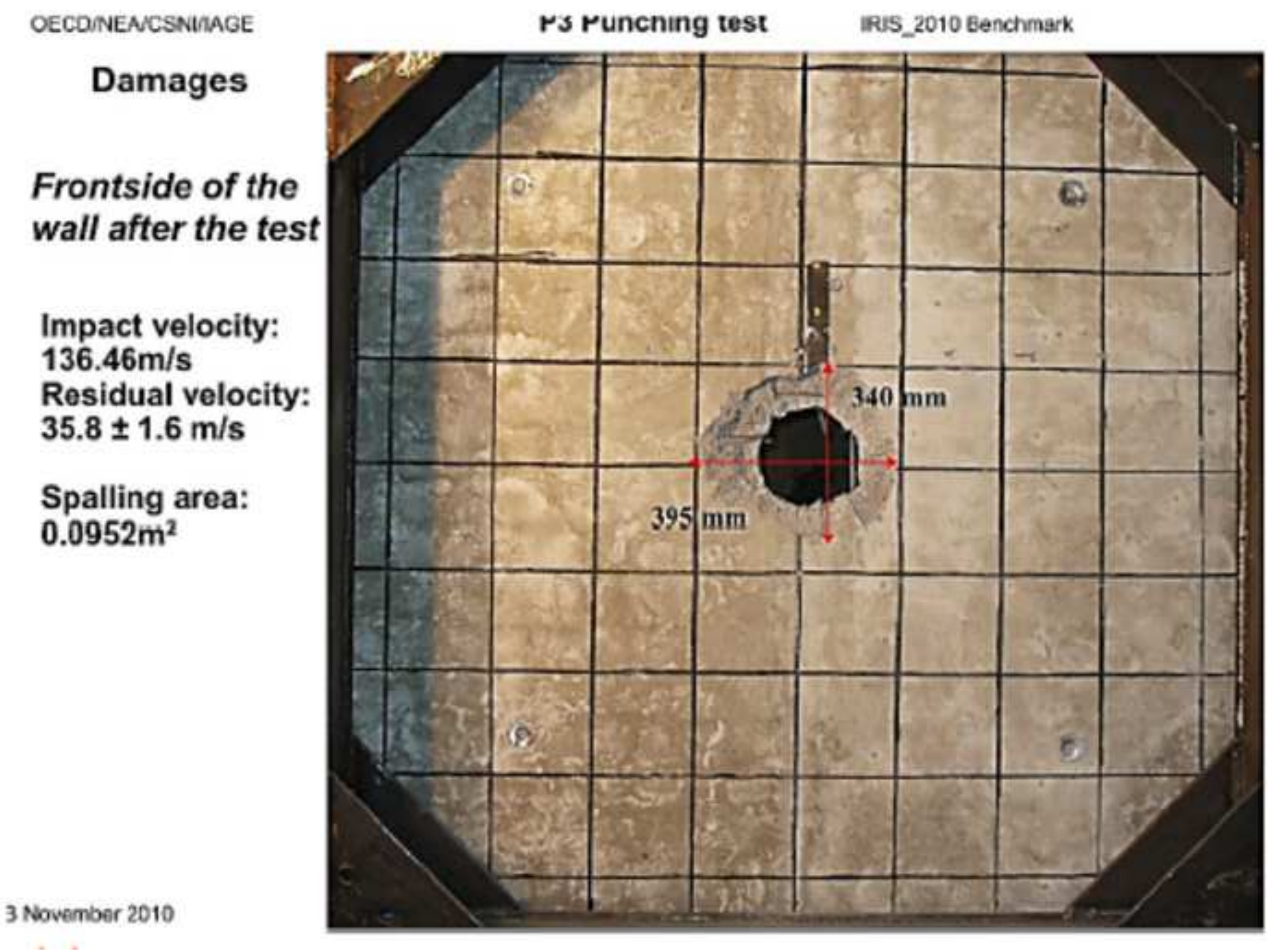

OECD/NEA/CSNI/IAGE

P3 Punching test

IRIS_2010 Benchmark

Damages

Frontside of the wall after the test

Impact velocity: 136.46m/s
Residual velocity: 35.8 ± 1.6 m/s

Spalling area: 0.0952m²

3 November 2010

Figure Click here to access/download;Figure;Fig5a.PNG

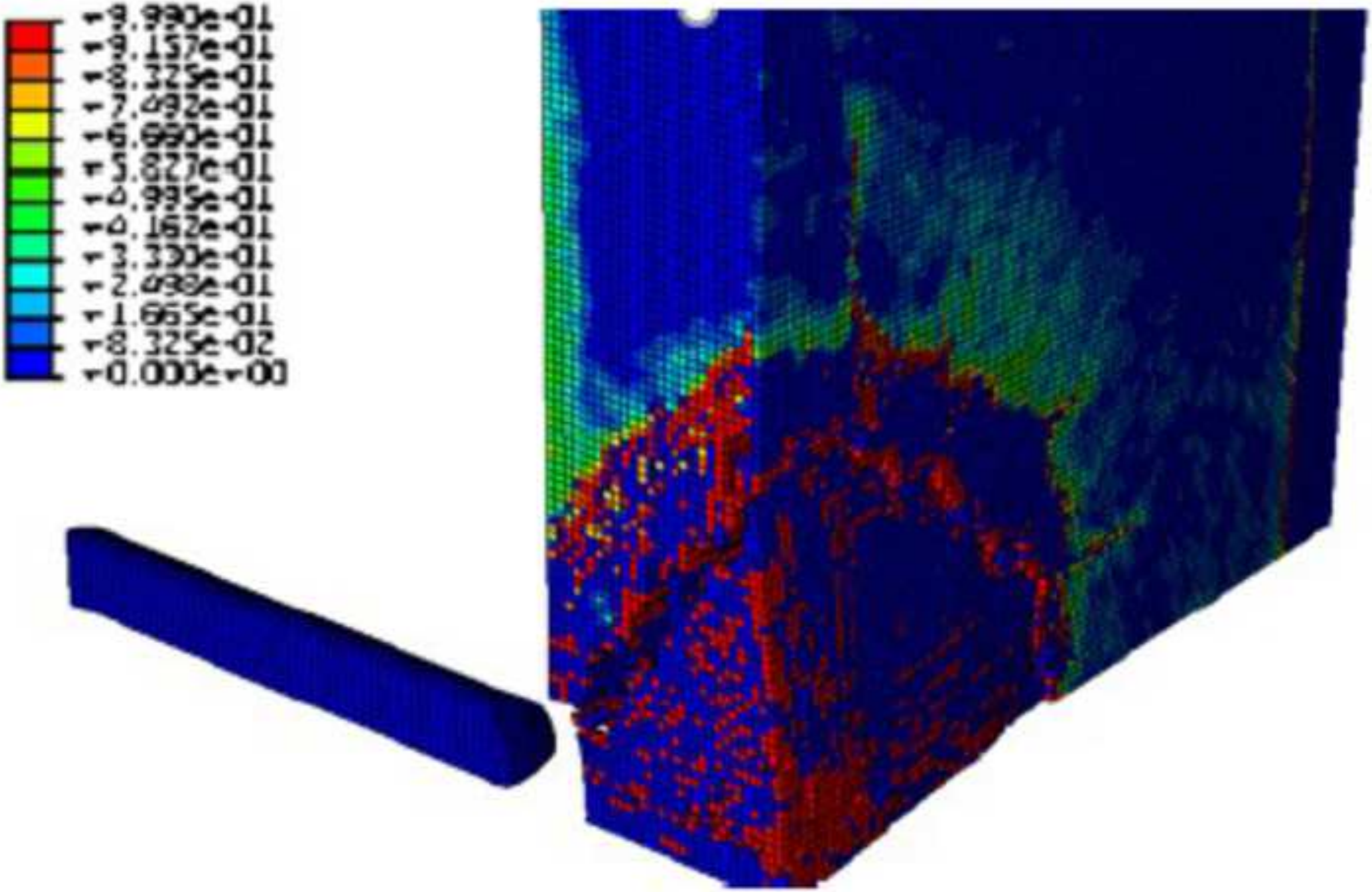

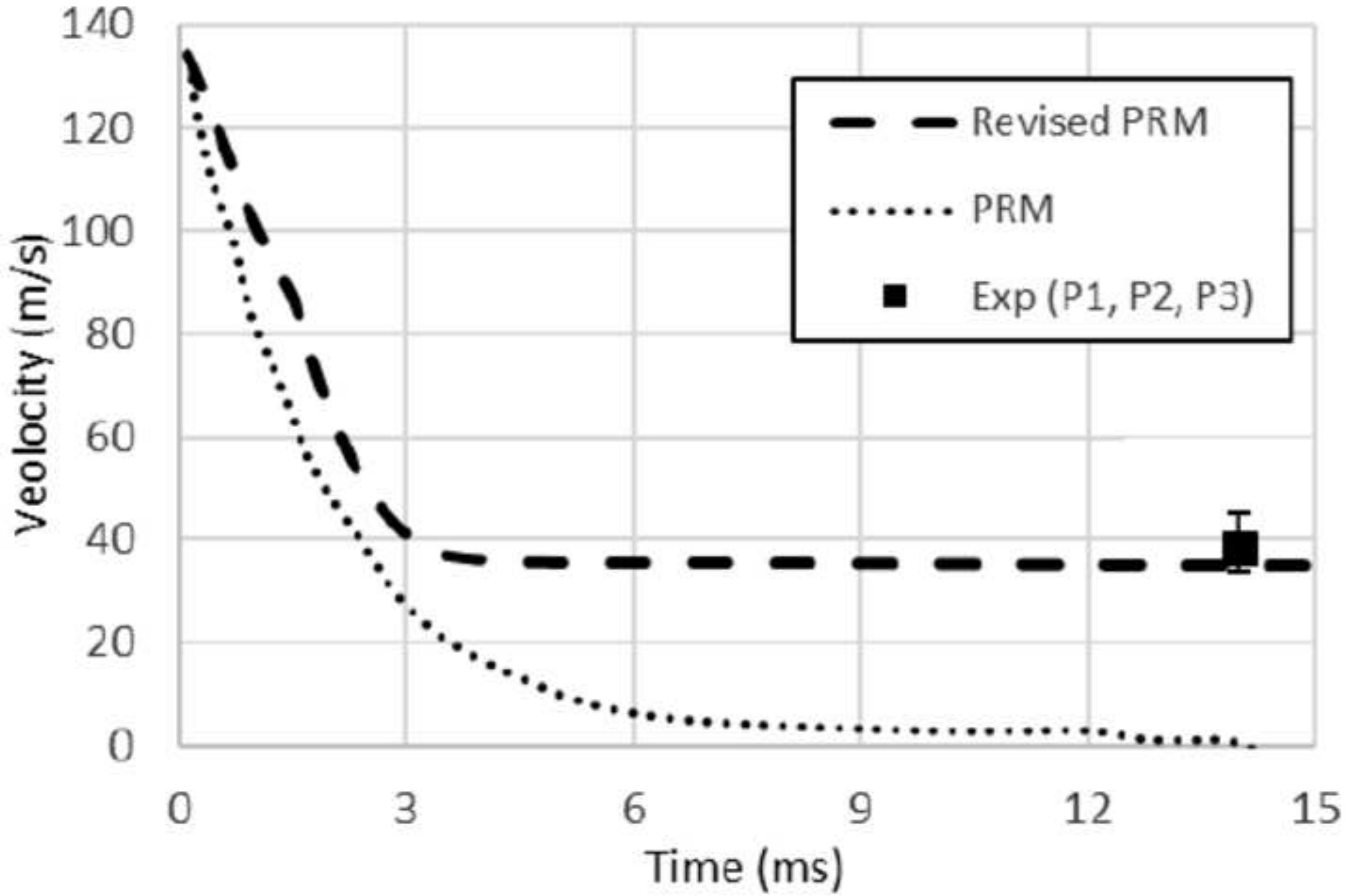
Veolocity (m/s)
140
120
100
80
60
40
20
0
0
3
6
9
12
15
Time (ms)
Revised PRM
PRM
Exp (P1, P2, P3)

Click here to access/download;Figure;Fig9.png